THE ASTROPHYSICAL JOURNAL, 406:319–345, 1993 March 20

ENERGY BALANCE IN THE SOLAR TRANSITION REGION. III. HELIUM EMISSION IN HYDROSTATIC, CONSTANT-ABUNDANCE MODELS WITH DIFFUSION

J. M. FONTENLA
University of Alabama in Huntsville, Huntsville, AL 35899
AND
E. H. AVRETT AND R. LOESER
Harvard-Smithsonian Center for Astrophysics, 60 Garden Street, Cambridge, MA 02138
Received 1992 April 2; accepted 1992 September 24

ABSTRACT

In our previous papers we described the mathematical formalism and the computed results for energy-balance hydrostatic models of the solar transition region. This region, characterized by a steep temperature gradient, is the interface between hot coronal material at 10^6 K and much cooler chromospheric material having temperatures at or below 10^4 K, and forms a narrow emission rim observed at the solar limb. In our model calculations we balance the radiative losses from the transition region with the total energy downflow at each depth in the atmosphere. The models include a detailed treatment of particle diffusion (in this case described by the ambipolar diffusion velocity), including the resulting departures from local ionization equilibrium and the transport of ionization energy. Our previous calculations of the hydrogen spectra agree reasonably well with the observed Lyα and Lyβ line intensities and profiles and account for the observed spatial variations of these lines. In this paper we discuss in some detail the limitations of the hydrostatic and one-dimensional assumptions used. Then we analyze the determination of helium emission when diffusion is included. We use transport coefficients estimated from kinetic theory to determine the helium departures from local ionization balance. We calculate the helium spectra for each of our models (A, C, F, and P) and evaluate the role of helium in the energy transport. Also, we investigate the effects of coronal illumination on the structure of the transition region and upper chromosphere, and show how coronal illumination affects various EUV lines and the He I 10830 Å line. Comparing with both absolute intensities and detailed line profiles, we show that our models are consistent not only with the observed hydrogen spectra but also with the available helium spectra.

Subject headings: diffusion — line: formation — Sun: transition region — Sun: UV radiation

1. INTRODUCTION

In our previous papers (Fontenla, Avrett, & Loeser 1990, 1991, hereafter Papers I and II) we focused on the problem of explaining the origin of the observed UV line emission of hydrogen (mainly Lyα). This line emission could not be explained by previous energy-balance models of the solar transition region that were based on energy transport by thermal conduction alone. The semiempirical models of Vernazza, Avrett, & Loeser (1981, hereafter VAL) required an ad hoc temperature plateau (and corresponding ad hoc local heating) to bring the integrated intensity into agreement with observations, but the calculated line profiles were not in good agreement with observed ones. We showed in our previous papers that the inclusion of particle diffusion (in the form of classical ambipolar diffusion) explains the energy balance of the low transition region, accounts for the integrated intensities, and brings the line profiles into better agreement with the observations.

In the present paper we continue to study the low transition region by evaluating the effects of diffusion on the formation of He I and He II spectra and on the energy balance. We also study in more detail the line profiles of the most significant lines, and we compare with some observations. Our models again correspond to different solar features and contain revised versions of the quiet-Sun models A, C, and F (see VAL; Avrett 1985) and the plage model P (see Paper II). The revisions made here are mainly in the temperature rise at the top of the chromosphere necessary to bring the wings of Lyα and the Lyman continuum into agreement with observations. These changes will be discussed in more detail below.

The present calculations are important not only for a theoretical understanding of the processes that produce the emission. They are also important for developing semiempirical diagnostics of the solar atmosphere and the atmospheres of other stars that have a transition region and a corona. Our results show that some emission features are clearly related to the energy flow through the transition region, some emissions or line components are determined by incident radiation from the corona, and others are determined by energy deposition in the chromosphere. Since there are well-known observed statistical relationships between the coronal radiation, the transition-region heat flux, and the chromospheric emissions, one can expect that to some extent the spatial and temporal averages of the emissions are related. But such statistical relationships are not very accurate and cannot be applied to spatially and temporally resolved observations. Studies based on model calculations can clarify many of these effects.

The formation of the He lines has been controversial for some time. Different ideas were proposed for the mechanism of excitation, and the controversy centered on collisional versus radiative excitation and ionization. However, all the model calculations published so far have failed to explain the observed intensities and profiles of the He I resonance lines. The usual models based on the emission measures cannot

explain how the thermal energy carried by electron conduction can reach the low transition region. Introducing a plateau region to explain the integrated intensities is compatible with energy balance only if an ad hoc local dissipation mechanism is introduced, but then the calculations show an extremely deep central reversal in the 584 Å line which does not seem consistent with the observations. The problem of explaining the He I resonance lines is then analogous to that of explaining the hydrogen Lyα line. As an alternative, Jordan (1975) suggested that different temperatures be used for computing the excitation and the local ionization. This is also an ad hoc solution, but it produces an effect similar to the one we found for hydrogen (see Paper I), viz., the degree of ionization of the region emitting the line center is lower than is predicted by local ionization balance.

Here we extend our previous studies of particle diffusion, an effect which has to be taken into account in the transition region between coronal and chromospheric material because of the steepness of the temperature and ionization gradients. We show that diffusion produces important departures from local helium ionization and thus increases the intensities of the helium lines (and particularly the line centers). The resulting intensities and profiles are generally consistent with current observations, but the absolute intensity of the He II 304 Å line is low compared with some observations. In our present models we assume a simplified model with the following constraints: a one-dimensional plane-parallel atmosphere in hydrostatic equilibrium, and approximate energy balance between the total downward heat flux and the radiative losses. These approximations constitute the first step in constructing detailed models aimed at an understanding of the physical processes in the transition region. In the next section we will explain the basis for our simplifications, which, although restrictive, are well suited to a description of most features of the solar atmosphere. Moreover, the processes we describe are likely to occur also in more complicated situations, as will be discussed.

We show that our models reproduce for the first time without ad hoc assumptions the resonance line profiles of helium as well as hydrogen in various solar features spanning several orders of magnitude in UV emission. Our models contain only a few free parameters that have been adjusted to fit the observations. The most critical parameter is the pressure at the base of the transition region, and this is related to the downward energy flux (see Paper II). The success of our models in fitting many more observations than the number of adjustable parameters at our disposal is an indication of the validity of our calculations, which are derived from well-established physical processes.

The equations for the diffusion of hydrogen and helium considered here are described in the next sections and are derived in the Appendix. We define a set of species diffusion velocities in the fluid frame (i.e., the diffusion velocities of the different species are relative to the frame of the local center of mass). These individual diffusion velocities are expressed in terms of a complete set of relative diffusion velocities which are computed from a first-order expansion of the distribution functions around the local Maxwellian. The relative diffusion velocities are expressed as linear functions of the relative concentration and temperature gradients (e.g., see Chapman & Cowling 1936; Braginskii 1965). In Paper I we explained how we obtained the diffusion coefficients in partially ionized pure hydrogen (ambipolar diffusion). Here we use these hydrogen coefficients without modification, since the helium number density is insufficient to produce very significant changes in the hydrogen diffusion. In the Appendix we show the way in which we have computed the relative diffusion coefficients for helium. The approach we use is based on the formalism of Schunk (1975) and Gueiss & Burgi (1986). However, the results have only order-of-magnitude accuracy because of some simplifying assumptions (e.g., the assumed dependence of the cross sections on velocity). Nevertheless, the coefficients used here are sufficient for determining the basic physical processes and calculating approximate values for the line intensities and profiles. In the present paper we are concerned with physical processes in the solar atmosphere and have not attempted to adjust atmospheric model parameters to match observed intensities and line profiles in detail.

In the following sections we discuss the procedures for constructing the models and for computing the helium spectra. We show the effects of changes in the parameters of the models, including the illumination by coronal line radiation. We also indicate how our calculated profiles agree with available observational data. Finally, we mention four basic problems in the current model calculations that arise in this study, and suggest possible solutions. The first problem arises because of the uncertain structure of the upper chromospheric layers of our current models; the second is the mismatch between the observation and calculation of the continuum around 1600 Å (which originates close to the temperature minimum); the third is the low intensity of the calculated He II 1640 Å line (He II Balmer-α). These three problems have implications for the interpretation of the observations. The fourth and probably most critical problem is the large outward decrease of the calculated helium abundance at the top of the chromosphere in our hydrostatic calculations. We find that (1) this decrease is induced by the effects of hydrogen ambipolar diffusion on the helium atoms and ions in the upper chromosphere and lower transition region and (2) such a decrease can be at least partially compensated by a small mass outflow of the magnitude of the solar wind. We suggest that the effect of hydrogen ambipolar diffusion may explain the observed low abundance of helium and other species with high first ionization potential in the corona and solar wind relative to their abundance in the photosphere and chromosphere.

2. THE ONE-DIMENSIONAL HYDROSTATIC MODEL

Our basic model of the transition region is a plane-parallel atmosphere in hydrostatic equilibrium having a distribution of temperature with height such that the energy radiated (mostly in EUV/UV lines) is balanced by the total particle-energy downflow from the corona. This downflow is dominated by electron conduction in the upper transition region and by hydrogen ionization-energy diffusive transport in the lower transition region (see Papers I and II). Our basic model calculation was described in detail in Papers I and II. In these papers we discussed the lower boundary conditions for the transition-region models determined from empirical chromospheric models, and we established a relationship between the pressure of the low transition region and the heat flux at its top. In Paper II we gave results for four models, A, C, F, and P, which correspond to faint, average, and bright regions of the quiet Sun, and a typical plage area. The underlying atmospheres in these models were obtained from semiempirical models mainly based on some visible and UV continua and lines. The photospheric and low chromospheric parts of the

models seem reasonably well defined, but the upper chromospheric parts of these models are less well defined because there were not as many observational constraints. One of the few visible lines formed (i.e., having optical depth unity) in the upper chromosphere is the central part of the hydrogen Balmer-α line, but the Balmer lines are mostly radiatively excited and are not very sensitive to the local temperature. Better diagnostics will be obtained by further studies of strong UV emission lines which are more sensitive to local conditions, e.g., the Mg II h and k line cores which are formed close to the top of the chromosphere (at around 8000 K and above). As a consequence of the present lack of knowledge of the detailed upper chromospheric structure, we must regard the models in this region as somewhat uncertain. The only important free parameter at the upper boundary of our transition-region models is the energy downflow. As explained in Paper II we require that the energy downflow be reduced to almost zero at the bottom of the transition region as the result of radiative losses. This is equivalent to specifying the energy downflow at the top and locating the transition region at a pressure such that all the downflowing energy is radiated away between the two boundaries. As we mentioned before, some residual energy flow exists at the base of the transition region in our models, determined by the temperature and its gradient at the top of the chromosphere. This residual flow is highly uncertain at present, but does not have a major effect on our transition-region models.

It is clear that our models constitute a very simplified picture of the solar transition region. Observations suggest that there is considerable roughness and variability of the solar transition region, and that there are magnetic loop structures of several sizes as well as regions of open magnetic fields. Also, flows have been found displaying mostly subsonic velocities, but rarely do supersonic flows appear. The line broadening that is observed suggests turbulent motions. Transient phenomena are observed that are called UV microflares. It can be argued that the existence of these phenomena may invalidate our models. However, we show in this section that our simplified models of the transition region can be used to interpret these observations in many cases. Indeed, many features of our models often apply wherever there is an interface between hot material, with temperature above 100,000 K, and cool material, with temperatures in the chromospheric range, whatever the physical location of such an interface.

The assumption of one-dimensional geometry in the calculation of the particle transport and radiative transfer is justified when the characteristic length of variation of all the relevant parameters (density, temperature, and ionization) in a particular direction (the direction of the stratification) is much smaller than that in the two perpendicular directions. This may occur for cases in which the vertical stratification, with or without a vertical magnetic field, occurs over short distances compared with horizontal variations. Consider, for instance, a footpoint of a coronal loop as shown in Figure 1. Here assume that there is a vertical field, which may vary between the inside and outside of the indicated cylindrical region. Let L be the horizontal size of the loop, and let us assume that the relevant physical parameters (density, temperature, ionization) are homogeneous over the horizontal extent of the cylinder. Comparing the horizontal size of the loop with the vertical extent, h, of the transition region we are computing, we find that in our one-dimensional models h is at most a few kilometers, the temperature scale height is typically a fraction of a kilometer, and the ionization scale height is about an order of magnitude smaller. In a vertical magnetic field the charged particle interactions are such that the particle transport fluxes are largely directed along the field. This occurs because the Larmor radius is typically small compared with the mean free path between collisions, and because of the vertical temperature variation. While neutral atoms are not directly affected by the field, they are strongly affected in the transition region by collisions with protons. The mean free path for neutral-proton collisions is typically a fraction of a kilometer (depending on the model). Consequently, the horizontal inhomogeneities will only be important for neutral particle transport when the variations have a characteristic horizontal length of no more than a few kilometers and are comparable to the vertical variations. Horizontal transport is thus not important, except at the edges, for features such as are shown in Figure 1, where the physical parameters remain homogeneous over distances L which greatly exceed h. In models of such features the parameters are more or less uniform over a horizontal distance L, while they change rapidly with height and rapidly across the feature boundary of width l. The effects of transverse inhomogeneity on radiative transfer will be important only when L is comparable to or smaller than h, i.e., if the horizontal scale of variations is less than a few kilometers. Otherwise, the radiative transfer across the sides of the cylinder shown in Figure 1 would be negligible. At present there is no evidence for such ultra–fine-scale structure (L less than 10 km); the smallest features that have been observed, the intergranular lanes in the photosphere, have dimensions of order 200 km. If one assumes that this is the typical size of the smallest horizontal structures of the solar transition region, the transverse structure would only be important in narrow layers at the edges of the otherwise transversely homogeneous structures. Consequently the plane-parallel approach is perfectly adequate for modeling purposes. For magnetic flux loops the effects of any reasonable increase of loop cross section with height are entirely negligible for low–transition-region models. In some cases it may be necessary to take into account the inclination of the magnetic field with respect to the direction of the temperature gradient, and this can be achieved approximately (except for angles very close to 90°) by reducing the charged particle heat flow by the squared cosine of the inclination angle, i.e., by neglecting the transport transverse to the magnetic field. At this point it is not clear what effects such an inclination of the field would have on ambipolar diffusion.

If the roughness of the solar surface is substantial, however, it may be necessary to correct for the fact that some of the radiation emitted by the transition regions located at greater heights would illuminate other transition regions below at smaller heights. The cool material in a few high loops (visible in Lyα, e.g., Fontenla, Reichmann, & Tandberg-Hanssen 1988)

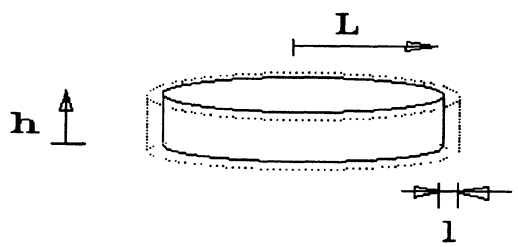

FIG. 1.—Schematic geometry of the footpoint of a hot coronal magnetic feature of radius L; h is the height of the transition region, and l is the thickness of the interface between this feature and its surroundings.

would scatter back (inward) part of the radiation emitted outward by the transition regions at lower altitudes. Radiative transfer in three dimensions is difficult to treat but has recently been addressed by Lindsey & Jefferies (1990). In our case the most significant transfer effects occur in the extreme ultraviolet (EUV) resonance lines which have large optical path lengths across horizontal inhomogeneities, so that only the vertical transfer of radiation is important.

The possible scenario for the layers above the chromosphere is shown in Figure 2, where we schematically indicate hot coronal loops (temperature $\sim 10^6$ K), intermediate temperature loops (temperature $\sim 10^5$ K), cool loops (temperature $\sim 10^4$ K), and cool prominence material. The properties of the regions between the features shown in the figure are mostly unknown. The magnetic field may be weaker or stronger, or these regions may be filled by other loops similar to the ones drawn but of much smaller density. For many loops, coronal temperatures predominate over the topmost portion of the loop, and transition regions occur at the footpoints where they join with the chromosphere. These transition regions occur at slightly different heights (see Paper II), and the corresponding loops have different maximum temperatures and large variations in density, depending on the energy dissipated throughout the whole loop. The thickness of the observed loops is probably a few hundred kilometers, and the heat transport occurs basically along the loop axis.

We now consider the validity of the hydrostatic conditions in our models. First we consider the possible effects of a magnetic field. It may be argued that there may be a substantial change in the magnetic pressure with height in a force-free field. Such a variation must be compensated by the magnetic tension because the force-free condition implies a vanishing Lorentz force (i.e., magnetic force). If electric currents occur in the upper chromosphere, transition region, or corona, violent motions would immediately occur that would relax the magnetic configuration, bringing the electric currents to field alignment, i.e., to a force-free configuration. Violent motions of this nature have been observed in solar flares, surges, prominence eruptions, and spicules and in UV jet and turbulent events. Despite the variety of such dynamic events, they constitute a relatively rare occurrence over most of the solar surface. Consequently, we find no basis for assuming any particular effects of the magnetic forces over the atmospheric stratification we compute; even where some small effects do occur, they are not sufficient to invalidate our basic assumptions. The effect of smaller, random velocities was accounted for in the chromospheric and photospheric layers in the form of turbulent velocities which slightly affect the height scale as described in the VAL papers. The treatment of these lower layers is beyond the scope of the present paper, but it constitutes an important topic for research. Here we are concerned only with the transition region, whose thickness is much smaller than the pressure scale height (even at the lowest temperature). As a consequence, our models contain a transition region which is basically isobaric, although a small variation of the gas pressure, p, occurs due to the turbulent velocity, V_t, just as in the lower layers. This variation is given by the Bernoulli law for incompressible fluids,

$$\Delta(p + \tfrac{1}{2}\rho V_t^2) = -g\rho\,\Delta z\,, \tag{1}$$

where z is the geometrical height, ρ is the mass density, and g is the gravitational acceleration. The use of an incompressible pressure structure for the transition region can be justified by considering that, even using the smallest sound speed, the sound transit time through this narrow region is only about 1 s or less. Consequently, any departures from the structure given by equation (1) would relax in less than a few seconds and are not important.

Considering other possible effects of departures from a stationary state in the transition region, we find that the characteristic time for reaching ionization balance is at most a few seconds. This can be estimated from the minimum of the mean ionization and recombination times and the time scale of a typical diffusion process, so that

$$t_{\rm dif} \approx (\Delta z)^2/D_x\,, \tag{2}$$

where D_x is the diffusion coefficient (eq. [4] in Paper II). The possible departures from energy balance can be estimated as the smaller of (a) the radiative cooling time,

$$t_{\rm rad} \approx 3p/2q_R\,, \tag{3}$$

where p is the gas pressure and q_R is the radiative loss term (see Paper I), and (b) the heat conduction time,

$$t_{\rm con} \approx 3p(\Delta z)^2/2K\,, \tag{4}$$

where K is the total heat flux coefficient (eq. [18] in Paper II). We conclude that the temperature relaxation time is at most a few seconds for the transition region. Consequently, if variations in the boundary conditions are applied, one expects that pressure, temperature, and ionization will all reach equilibrium quickly (in a few seconds), and only variations with characteristic times less than a few seconds may produce any significant departures from the equilibrium values. For the observed time scales of many seconds, the situation is not really stationary because all parameters are evolving in time. But for the purpose of the computations at any particular time, one can neglect the time derivatives in the equations (as we do in our model calculations). These conditions are customarily called "quasi-stationary" because all quantities can be obtained from the equations and boundary conditions at any given time, neglecting the time derivatives, but the physical quantities change in time as the boundary conditions evolve. Of course, this scheme does not apply to the chromospheric or coronal

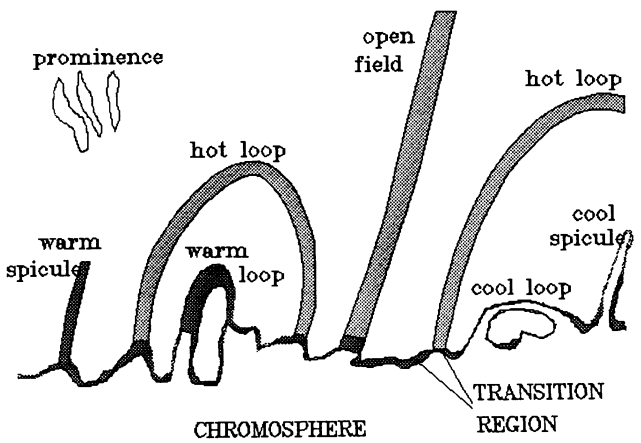

FIG. 2.—Sketch indicating some of the magnetic structures observed in the low corona. We show cool material (about 10^4 K) in the chromosphere and also in spicules, loops, and prominence material; warm material (about 10^5 K) in the transition region including loops and spicules; and hot material (about 10^6 K) in the loops and open fields.

layers in which some of the characteristic times (e.g., cooling and ionization relaxation times) are longer, of the order of few minutes.

A more serious problem for our current models may be posed by the moderate mass flow velocities which were included in our equations of Papers I and II, and in this paper, but have not been included in the numerical results we have presented so far. The effects of moderate mass motions can be relevant for the ionization balance and energy transport as was described in Paper I. But the effects appear only if the motions imply an effective differential velocity throughout the transition region, i.e., if the velocity varies with height so that a gas parcel experiences compression or expansion. If, on the other hand, the transition region is displaced as a whole, no effects are to be expected in this region apart from the general translation. We explained in Paper I that there is not a clear basis for assigning any particular velocity structure to the lower transition region, and available observations of the hydrogen and helium lines have not revealed Doppler shifts substantially different from those which can be expected from diffusion alone (see Paper II), except in rare cases as mentioned above. It is well known, however, that Doppler redshifts corresponding to about 7 km s^{-1} are observed in hotter lines, e.g., in the C IV 1548 Å line. We have not yet studied such highly ionized species and cannot answer whether there is a true "mass" downflow or just downward diffusion of C IV, and how mass is restored in the case of a true mass downflow. Potentially important effects of velocities which are within the range allowed by the available observations will be explored in future papers. In the present paper we will only consider them in relation to a critical problem concerning the variation of the helium abundance through the transition region. Another velocity effect to consider is the "microturbulent" velocity V_t used in equation (1), determined from heavy-particle Doppler line widths that are greater than the thermal widths corresponding to the local electron temperature. The excess width could be attributed to a heavy-species temperature that is higher than the electron temperature, but it is usually considered to be the result of a distribution of unresolved fine-structure elements or "eddies" having a Gaussian distribution of random velocities. This explanation assumes that the scale size of the velocity variations is much larger than the heavy-particle mean free path (which is a few kilometers in the low transition region).

The character of this "microturbulence" and its role in the energetics and diffusion are poorly understood. Cally (1990) shows that under several assumptions turbulence may substantially enhance the energy flow in the transition region. Turbulent motions are well known to produce diffusion effects in many cases. Our calculations do not include turbulence, other than as a turbulent pressure in the hydrostatic equilibrium equation (see eq. [1] and § 4), because the transport properties of physical turbulence depend critically on the asymmetry of the eddy velocity distribution and on unknown parameters such as the "mixing length." Since it is difficult to infer specific values of such parameters from theory, we ignore these effects, except to keep in mind that they usually tend to increase the "effective" transport coefficients.

3. THE CALCULATIONS

As explained in Papers I and II, we use the energy-balance equations to determine the transition region corresponding to a given underlying chromosphere. The chromospheric models here are slightly different from those used in Paper II. The differences are a slight increase in the temperature structure of the top of the chromosphere which we have introduced to explain the wings of the Lyα line. These temperature changes are relatively small, but they help to increase the line width and the height of the red and blue peaks. Later in this paper we will compare the computed profiles with the observations and will explain how the small change in the models improves the agreement between the computed and observed profiles. For reference, we list in Tables 1–4 the atmospheric parameters for models A, C, F, and P. In addition to the hydrogen calculations described in Papers I and II, we now also solve the statistical equilibrium and radiative transfer equations for a model He I atom with 13 bound levels and a model He II atom with six bound levels. The He I atom includes all singlet and triplet energy levels to $4p$, with 22 radiative transitions, and the He II atom includes all levels and transitions to $n = 6$. We include the He I transition-region lines at 584 and 537 Å and upper chromospheric 10830 and 5875 Å lines, and the important He II lines at 304 Å (He II Lyα) and 1640 Å (He II Balmer-α). The He I and He II continua shortward of 504 and 228 Å are also calculated in detail, including the interaction between these continua and the hydrogen Lyman continuum. We also include the radiation shining down from the corona upon the transition region and upper chromosphere. As discussed later, this radiation is the coronal component of the solar EUV irradiance according to Tobiska (1991).

The hydrogen diffusion equations were solved as described in Papers I and II. Here we neglect the relatively small effect on hydrogen diffusion due to helium. The diffusion of helium, however, is strongly affected by collisions with hydrogen atoms and ions. These collisions affect the coefficients and also produce helium diffusion induced by the hydrogen diffusion.

The main collisional interaction between protons and hydrogen atoms is elastic charge exchange (see Paper I). Hydrogen excitation by protons is negligible compared with electron collisional excitation (see Janev et al. 1987). Excitation of helium by protons and heavier particles also is negligible in the temperature and density range of our calculations.

3.1. *Helium Diffusion*

We describe in this section the formalism used for our calculations of helium diffusion, and the solution of the statistical equilibrium equations including this diffusion. In an Appendix we describe in some detail the transport equations and the elastic collision cross sections we have used for estimating the diffusion coefficients. We give the equations that include the time derivatives in the full three-dimensional case with mass velocity, but except for turbulent pressure, our present calculations are restricted to hydrostatic time-independent, one-dimensional cases.

We define the diffusion velocities of the different types of particles with respect to the center of mass, which moves with a velocity U. In this center-of-mass frame, i.e., "fluid frame," we consider the velocities V_e, V_p, V_a, $V_{\rm I}$, $V_{\rm II}$, $V_{\rm III}$, corresponding to electrons, protons, hydrogen atoms, and neutral, singly ionized, and doubly ionized helium, respectively. The corresponding number densities are given by n_e, n_p, n_a, $n_{\rm I}$, $n_{\rm II}$, $n_{\rm III}$, and the total species number densities are

$$n_{\rm H} = n_p + n_a\,, \quad n_{\rm He} = n_{\rm I} + n_{\rm II} + n_{\rm III}\,. \tag{5}$$

From the conservation of hydrogen and helium atoms it follows that

$$\frac{\partial n_{\rm H}}{\partial t} + \nabla \cdot F_{\rm H} = 0\,, \quad \frac{\partial n_{\rm He}}{\partial t} + \nabla \cdot F_{\rm He} = 0\,, \tag{6}$$

TABLE 1

MODEL A

	Depth (km)	Temp. (K)	Electron	Proton	H(1)	H(2)	He(1)	He(2)	HeII	HeIII
			number density in (/cm**3)							
1	-2276.73	102770	3.32E+09	2.77E+09	6.05E+04	9.15E-03	5.54E+02	3.12E-01	1.11E+07	2.66E+08
2	-2273.96	98790	3.44E+09	2.89E+09	1.08E+05	1.60E-02	1.51E+03	8.23E-01	2.47E+07	2.63E+08
3	-2271.36	94800	3.58E+09	3.01E+09	1.68E+05	2.46E-02	3.48E+03	1.87E+00	4.13E+07	2.58E+08
4	-2268.95	90816	3.72E+09	3.14E+09	2.70E+05	3.93E-02	7.69E+03	4.03E+00	6.04E+07	2.52E+08
5	-2265.13	83891	4.00E+09	3.41E+09	6.65E+05	9.57E-02	2.71E+04	1.32E+01	1.03E+08	2.34E+08
6	-2261.33	75934	4.37E+09	3.77E+09	2.11E+06	3.00E-01	1.12E+05	4.73E+01	1.69E+08	2.02E+08
7	-2259.42	71336	4.62E+09	4.02E+09	4.38E+06	6.24E-01	2.64E+05	9.95E+01	2.15E+08	1.81E+08
8	-2257.48	66145	4.94E+09	4.33E+09	9.24E+06	1.33E+00	6.31E+05	2.02E+02	2.70E+08	1.59E+08
9	-2255.52	60170	5.38E+09	4.75E+09	2.02E+07	3.01E+00	1.58E+06	3.97E+02	3.36E+08	1.37E+08
10	-2253.56	53284	6.00E+09	5.33E+09	4.55E+07	7.28E+00	4.16E+06	7.17E+02	4.11E+08	1.22E+08
11	-2252.58	49385	6.43E+09	5.72E+09	7.04E+07	1.19E+01	6.99E+06	9.28E+02	4.51E+08	1.19E+08
12	-2251.65	45416	6.92E+09	6.17E+09	1.07E+08	1.92E+01	1.16E+07	1.14E+03	4.95E+08	1.20E+08
13	-2250.73	41178	7.55E+09	6.74E+09	1.62E+08	3.13E+01	1.95E+07	1.28E+03	5.44E+08	1.23E+08
14	-2249.79	36594	8.38E+09	7.48E+09	2.47E+08	5.22E+01	3.34E+07	1.25E+03	6.04E+08	1.31E+08
15	-2248.90	32145	9.37E+09	8.38E+09	3.69E+08	8.48E+01	5.60E+07	1.04E+03	6.71E+08	1.41E+08
16	-2248.05	27972	1.05E+10	9.45E+09	5.37E+08	1.32E+02	9.06E+07	7.38E+02	7.46E+08	1.53E+08
17	-2247.21	24056	1.20E+10	1.07E+10	7.67E+08	1.99E+02	1.39E+08	4.90E+02	8.37E+08	1.61E+08
18	-2246.33	20416	1.37E+10	1.23E+10	1.09E+09	2.95E+02	2.18E+08	4.06E+02	9.43E+08	1.61E+08
19	-2245.61	17925	1.51E+10	1.37E+10	1.43E+09	3.93E+02	3.29E+08	4.43E+02	1.02E+09	1.44E+08
20	-2244.89	15941	1.65E+10	1.51E+10	1.84E+09	5.09E+02	4.60E+08	5.22E+02	1.10E+09	1.19E+08
21	-2243.80	13897	1.81E+10	1.68E+10	2.59E+09	7.17E+02	6.98E+08	6.38E+02	1.16E+09	7.11E+07
22	-2242.54	12650	1.90E+10	1.78E+10	3.59E+09	9.97E+02	9.81E+08	6.80E+02	1.11E+09	3.77E+07
23	-2239.42	11650	1.88E+10	1.78E+10	6.18E+09	1.74E+03	1.54E+09	5.54E+02	8.49E+08	1.29E+07
24	-2235.00	11100	1.76E+10	1.68E+10	9.66E+09	2.74E+03	1.88E+09	4.91E+02	7.59E+08	6.54E+06
25	-2200.00	10250	1.65E+10	1.55E+10	1.71E+10	4.70E+03	2.31E+09	6.21E+02	9.45E+08	7.33E+06
26	-2167.00	9750	1.69E+10	1.58E+10	2.17E+10	5.18E+03	2.73E+09	7.06E+02	1.02E+09	6.55E+06
27	-2149.00	9500	1.71E+10	1.59E+10	2.46E+10	5.27E+03	2.99E+09	7.54E+02	1.06E+09	6.59E+06
28	-2126.00	9200	1.72E+10	1.60E+10	2.89E+10	5.32E+03	3.37E+09	8.14E+02	1.12E+09	6.87E+06
29	-2108.00	9000	1.73E+10	1.60E+10	3.26E+10	5.33E+03	3.70E+09	8.59E+02	1.16E+09	6.87E+06
30	-2074.00	8600	1.73E+10	1.59E+10	4.10E+10	5.40E+03	4.45E+09	9.50E+02	1.24E+09	7.00E+06
31	-2050.00	8300	1.73E+10	1.59E+10	4.82E+10	5.48E+03	5.12E+09	1.02E+03	1.29E+09	7.22E+06
32	-2022.00	7950	1.73E+10	1.59E+10	5.82E+10	5.68E+03	6.06E+09	1.09E+03	1.35E+09	7.02E+06
33	-1988.00	7650	1.74E+10	1.58E+10	7.16E+10	5.98E+03	7.36E+09	1.13E+03	1.38E+09	6.69E+06
34	-1960.00	7450	1.74E+10	1.59E+10	8.40E+10	6.30E+03	8.61E+09	1.15E+03	1.38E+09	6.39E+06
35	-1910.00	7180	1.78E+10	1.63E+10	1.10E+11	7.00E+03	1.13E+10	1.12E+03	1.31E+09	5.46E+06
36	-1870.00	7060	1.83E+10	1.68E+10	1.35E+11	7.67E+03	1.40E+10	1.05E+03	1.21E+09	4.58E+06
37	-1785.00	6850	1.97E+10	1.84E+10	2.08E+11	9.57E+03	2.17E+10	8.72E+02	9.54E+08	2.89E+06
38	-1675.00	6650	2.25E+10	2.13E+10	3.66E+11	1.32E+04	3.81E+10	6.90E+02	6.55E+08	1.37E+06
39	-1575.00	6480	2.55E+10	2.44E+10	6.25E+11	1.75E+04	6.45E+10	5.51E+02	5.08E+08	6.20E+05
40	-1475.00	6320	2.84E+10	2.74E+10	1.09E+12	2.22E+04	1.12E+11	3.68E+02	3.18E+08	1.50E+05
41	-1375.00	6150	3.10E+10	2.99E+10	1.96E+12	2.68E+04	1.99E+11	2.41E+02	2.87E+08	1.56E+04
42	-1275.00	5990	3.29E+10	3.17E+10	3.64E+12	3.09E+04	3.67E+11	1.21E+02	1.32E+08	9.85E+02
43	-1175.00	5820	3.47E+10	3.30E+10	7.06E+12	3.44E+04	7.10E+11	8.32E+01	5.33E+07	1.48E+02
44	-1075.00	5660	3.62E+10	3.34E+10	1.43E+13	3.69E+04	1.43E+12	6.28E+01	3.85E+07	3.66E+01
45	-975.00	5480	3.75E+10	3.26E+10	3.01E+13	3.78E+04	3.01E+12	3.35E+01	1.95E+07	4.55E+00
46	-900.00	5300	3.64E+10	2.83E+10	5.46E+13	3.24E+04	5.46E+12	1.56E+01	9.04E+06	4.61E-01
47	-850.00	5150	3.47E+10	2.29E+10	8.30E+13	2.54E+04	8.30E+12	9.51E+00	5.47E+06	9.21E-02
48	-800.00	4910	3.20E+10	1.39E+10	1.31E+14	1.48E+04	1.31E+13	7.26E+00	4.22E+06	3.12E-02
49	-750.00	4680	3.44E+10	6.62E+09	2.12E+14	7.84E+03	2.12E+13	5.59E+00	3.03E+06	8.81E-03
50	-700.00	4510	4.68E+10	3.07E+09	3.45E+14	5.10E+03	3.45E+13	3.46E+00	1.52E+06	1.22E-03
51	-650.00	4390	7.14E+10	1.67E+09	5.66E+14	4.39E+03	5.67E+13	1.57E+00	5.44E+05	8.70E-05
52	-600.00	4280	1.13E+11	9.51E+08	9.43E+14	4.14E+03	9.43E+13	6.27E-01	1.73E+05	4.52E-06
53	-550.00	4240	1.80E+11	7.70E+08	1.56E+15	5.56E+03	1.56E+14	2.82E-01	6.54E+04	2.20E-07
54	-525.00	4240	2.26E+11	7.70E+08	2.00E+15	7.14E+03	2.00E+14	1.75E-01	3.72E+04	4.16E-08
55	-500.00	4260	2.84E+11	8.55E+08	2.55E+15	1.01E+04	2.55E+14	9.35E-02	1.89E+04	6.64E-09
56	-450.00	4320	4.47E+11	1.19E+09	4.11E+15	2.28E+04	4.11E+14	1.61E-02	2.41E+03	6.52E-11
57	-400.00	4420	7.00E+11	2.13E+09	6.51E+15	6.41E+04	6.51E+14	6.52E-04	9.39E+01	6.35E-14
58	-350.00	4560	1.09E+12	4.89E+09	1.01E+16	2.19E+05	1.01E+15	5.08E-06	5.92E-01	1.66E-18
59	-300.00	4680	1.69E+12	1.05E+10	1.55E+16	6.50E+05	1.55E+15	1.54E-06	9.23E-03	8.80E-24
60	-250.00	4820	2.60E+12	2.76E+10	2.34E+16	2.03E+06	2.34E+15	9.56E-06	4.46E-02	2.61E-27
61	-200.00	4970	3.97E+12	8.47E+10	3.47E+16	6.32E+06	3.47E+15	6.76E-05	2.80E-01	3.64E-32
62	-150.00	5150	6.13E+12	3.04E+11	5.03E+16	2.11E+07	5.04E+15	5.71E-04	2.31E+00	3.15E-37
63	-100.00	5410	9.96E+12	1.39E+12	7.07E+16	8.93E+07	7.08E+15	7.44E-03	3.30E+01	9.49E-42
64	-50.00	5790	1.97E+13	7.47E+12	9.51E+16	5.05E+08	9.52E+15	1.65E-01	8.05E+02	2.07E-37
65	0.00	6520	7.67E+13	5.99E+13	1.18E+17	6.16E+09	1.18E+16	1.71E+01	7.30E+04	1.04E-30
66	20.00	6980	1.73E+14	1.53E+14	1.24E+17	2.14E+10	1.24E+16	1.83E+02	6.84E+05	2.83E-27
67	40.00	7590	4.47E+14	4.24E+14	1.27E+17	8.59E+10	1.28E+16	2.65E+03	8.35E+06	2.18E-23
68	60.00	8220	1.05E+15	1.02E+15	1.29E+17	2.89E+11	1.30E+16	2.75E+04	7.38E+07	5.49E-20
69	80.00	8860	2.21E+15	2.18E+15	1.30E+17	8.20E+11	1.32E+16	2.11E+05	4.88E+08	4.96E-17
70	100.00	9400	3.86E+15	3.82E+15	1.31E+17	1.78E+12	1.35E+16	9.55E+05	1.98E+09	7.58E-15

TABLE 2

MODEL C

	Depth (km)	Temp. (K)	Electron	Proton	H(1)	H(2)	He(1)	He(2)	HeII	HeIII
			number density in (/cm**3)							
1	-2219.43	102770	6.56E+09	5.48E+09	1.11E+05	3.70E-02	4.32E+02	5.98E-01	2.01E+07	5.28E+08
2	-2217.88	98790	6.81E+09	5.70E+09	1.79E+05	5.90E-02	1.20E+03	1.54E+00	4.41E+07	5.26E+08
3	-2216.43	94800	7.07E+09	5.94E+09	2.46E+05	8.00E-02	2.86E+03	3.39E+00	7.28E+07	5.22E+08
4	-2215.08	90816	7.36E+09	6.21E+09	3.44E+05	1.11E-01	6.72E+03	7.25E+00	1.05E+08	5.17E+08
5	-2212.92	83891	7.91E+09	6.73E+09	7.00E+05	2.20E-01	2.64E+04	2.44E+01	1.77E+08	4.98E+08
6	-2210.75	75934	8.66E+09	7.45E+09	2.05E+06	6.29E-01	1.25E+05	9.42E+01	2.90E+08	4.59E+08
7	-2209.65	71336	9.17E+09	7.94E+09	4.39E+06	1.33E+00	3.29E+05	2.15E+02	3.70E+08	4.28E+08
8	-2208.53	66145	9.82E+09	8.56E+09	9.81E+06	2.97E+00	8.62E+05	4.69E+02	4.75E+08	3.86E+08
9	-2207.40	60170	1.07E+10	9.41E+09	2.31E+07	7.09E+00	2.36E+06	9.92E+02	6.13E+08	3.33E+08
10	-2206.27	53284	1.19E+10	1.06E+10	5.70E+07	1.83E+01	6.75E+06	1.93E+03	7.90E+08	2.73E+08
11	-2205.70	49385	1.28E+10	1.14E+10	9.34E+07	3.12E+01	1.19E+07	2.61E+03	8.92E+08	2.47E+08
12	-2205.18	45416	1.38E+10	1.23E+10	1.47E+08	5.19E+01	2.03E+07	3.28E+03	9.98E+08	2.30E+08
13	-2204.66	41178	1.51E+10	1.35E+10	2.32E+08	8.80E+01	3.46E+07	3.76E+03	1.12E+09	2.22E+08
14	-2204.13	36594	1.67E+10	1.50E+10	3.69E+08	1.53E+02	6.05E+07	3.75E+03	1.26E+09	2.21E+08
15	-2203.63	32145	1.88E+10	1.69E+10	5.70E+08	2.61E+02	1.02E+08	3.14E+03	1.41E+09	2.27E+08
16	-2203.16	27972	2.12E+10	1.91E+10	8.50E+08	4.23E+02	1.64E+08	2.26E+03	1.59E+09	2.33E+08
17	-2202.70	24056	2.41E+10	2.18E+10	1.24E+09	6.62E+02	2.50E+08	1.52E+03	1.81E+09	2.36E+08
18	-2202.22	20416	2.77E+10	2.51E+10	1.78E+09	1.02E+03	3.89E+08	1.30E+03	2.07E+09	2.22E+08
19	-2201.83	17925	3.08E+10	2.81E+10	2.35E+09	1.40E+03	5.82E+08	1.43E+03	2.26E+09	1.90E+08
20	-2201.56	16500	3.29E+10	3.01E+10	2.82E+09	1.72E+03	7.45E+08	1.60E+03	2.38E+09	1.66E+08
21	-2201.16	15000	3.53E+10	3.25E+10	3.60E+09	2.26E+03	9.94E+08	1.85E+03	2.48E+09	1.26E+08
22	-2200.84	14250	3.65E+10	3.38E+10	4.28E+09	2.75E+03	1.20E+09	1.98E+03	2.50E+09	1.00E+08
23	-2200.10	13500	3.73E+10	3.47E+10	5.89E+09	4.00E+03	1.61E+09	2.01E+03	2.40E+09	5.57E+07
24	-2199.00	13000	3.72E+10	3.48E+10	8.24E+09	5.99E+03	2.05E+09	1.91E+03	2.21E+09	4.48E+07
25	-2190.00	12000	3.56E+10	3.30E+10	1.71E+10	1.78E+04	2.53E+09	2.23E+03	2.45E+09	3.07E+07
26	-2168.00	11150	3.81E+10	3.54E+10	2.12E+10	2.59E+04	3.03E+09	2.62E+03	2.60E+09	2.82E+07
27	-2140.00	10550	4.06E+10	3.77E+10	2.63E+10	2.96E+04	3.63E+09	3.00E+03	2.75E+09	2.66E+07
28	-2110.00	9900	4.24E+10	3.92E+10	3.54E+10	3.15E+04	4.48E+09	3.49E+03	2.96E+09	2.58E+07
29	-2087.00	9450	4.31E+10	3.98E+10	4.45E+10	3.23E+04	5.28E+09	3.85E+03	3.14E+09	2.53E+07
30	-2075.00	9200	4.34E+10	4.00E+10	5.03E+10	3.27E+04	5.78E+09	4.05E+03	3.23E+09	2.51E+07
31	-2062.00	8950	4.36E+10	4.01E+10	5.70E+10	3.32E+04	6.37E+09	4.27E+03	3.33E+09	2.49E+07
32	-2043.00	8700	4.37E+10	4.01E+10	6.69E+10	3.40E+04	7.25E+09	4.50E+03	3.44E+09	2.44E+07
33	-2017.00	8400	4.39E+10	4.01E+10	8.18E+10	3.54E+04	8.64E+09	4.74E+03	3.54E+09	2.33E+07
34	-1980.00	8050	4.42E+10	4.03E+10	1.06E+11	3.80E+04	1.11E+10	4.91E+03	3.56E+09	2.09E+07
35	-1915.00	7650	4.54E+10	4.19E+10	1.57E+11	4.37E+04	1.68E+10	4.54E+03	3.15E+09	1.43E+07
36	-1860.00	7450	4.70E+10	4.41E+10	2.12E+11	4.96E+04	2.32E+10	3.73E+03	2.52E+09	8.69E+06
37	-1775.00	7250	5.08E+10	4.87E+10	3.31E+11	6.13E+04	3.66E+10	2.34E+02	1.49E+09	3.07E+06
38	-1670.00	7050	5.74E+10	5.58E+10	5.74E+11	8.01E+04	6.22E+10	1.27E+03	8.55E+08	8.87E+05
39	-1580.00	6900	6.32E+10	6.16E+10	9.28E+11	9.69E+04	9.84E+10	7.78E+02	5.58E+08	3.49E+05
40	-1475.00	6720	7.04E+10	6.89E+10	1.66E+12	1.18E+05	1.72E+11	3.74E+02	2.21E+08	7.23E+04
41	-1378.00	6560	7.86E+10	7.66E+10	2.89E+12	1.42E+05	2.97E+11	2.87E+02	2.64E+08	1.10E+04
42	-1278.00	6390	8.76E+10	8.53E+10	5.30E+12	1.69E+05	5.39E+11	2.45E+02	2.27E+08	5.69E+03
43	-1180.00	6230	9.80E+10	9.50E+10	9.92E+12	2.00E+05	1.00E+12	1.69E+02	9.32E+07	2.87E+02
44	-1065.00	6040	1.10E+11	1.05E+11	2.15E+13	2.35E+05	2.16E+12	1.24E+02	4.86E+07	3.79E+01
45	-980.00	5900	1.18E+11	1.10E+11	3.92E+13	2.63E+05	3.93E+12	9.55E+01	3.58E+07	1.00E+01
46	-905.00	5755	1.23E+11	1.11E+11	6.79E+13	2.74E+05	6.80E+12	7.27E+01	2.62E+07	2.86E+00
47	-855.00	5650	1.24E+11	1.09E+11	9.92E+13	2.70E+05	9.93E+12	6.11E+01	2.12E+07	1.27E+00
48	-805.00	5490	1.08E+11	8.54E+10	1.48E+14	2.12E+05	1.48E+13	5.61E+01	2.04E+07	7.41E-01
49	-755.00	5280	9.41E+10	6.18E+10	2.27E+14	1.38E+05	2.27E+13	5.15E+01	1.92E+07	3.64E-01
50	-705.00	5030	8.28E+10	3.49E+10	3.56E+14	7.10E+04	3.56E+13	4.16E+01	1.56E+07	1.30E-01
51	-650.00	4750	9.03E+10	1.35E+10	6.03E+14	3.16E+04	6.03E+13	2.27E+01	7.82E+06	1.71E-02
52	-600.00	4550	1.26E+11	5.46E+09	9.89E+14	1.86E+04	9.89E+13	1.16E+01	3.20E+06	1.34E-03
53	-560.00	4430	1.77E+11	2.97E+09	1.48E+15	1.49E+04	1.48E+14	6.46E+00	1.57E+06	1.36E-04
54	-525.00	4400	2.41E+11	2.57E+09	2.08E+15	1.80E+04	2.08E+14	3.19E+00	7.16E+05	1.39E-05
55	-490.00	4410	3.28E+11	2.76E+09	2.90E+15	2.67E+04	2.90E+14	1.24E+00	2.45E+05	9.78E-07
56	-450.00	4460	4.66E+11	3.73E+09	4.19E+15	5.15E+04	4.19E+14	2.45E-01	4.32E+04	2.02E-08
57	-400.00	4560	7.24E+11	6.70E+09	6.54E+15	1.42E+05	6.55E+14	1.05E-02	1.61E+03	1.83E-11
58	-350.00	4660	1.12E+12	1.21E+10	1.01E+16	3.80E+05	1.01E+15	7.75E-05	9.95E+00	4.60E-16
59	-300.00	4770	1.71E+12	2.38E+10	1.54E+16	1.04E+06	1.54E+15	4.36E-06	3.44E-02	5.37E-22
60	-250.00	4880	2.60E+12	4.94E+10	2.33E+16	2.73E+06	2.33E+15	1.93E-05	1.02E-01	9.57E-26
61	-200.00	4990	3.93E+12	1.10E+11	3.47E+16	6.95E+06	3.48E+15	8.78E-05	3.90E-01	8.33E-31
62	-150.00	5150	6.04E+12	3.22E+11	5.05E+16	2.12E+07	5.06E+15	5.80E-04	2.43E+00	5.47E-36
63	-100.00	5410	9.89E+12	1.40E+12	7.10E+16	8.96E+07	7.11E+15	7.40E-03	3.33E+01	4.38E-41
64	-50.00	5790	1.97E+13	7.49E+12	9.55E+16	5.07E+08	9.56E+15	1.65E-01	8.07E+02	2.03E-37
65	0.00	6520	7.68E+13	6.00E+13	1.18E+17	6.18E+09	1.18E+16	1.71E+01	7.31E+04	1.04E-30
66	20.00	6980	1.73E+14	1.53E+14	1.24E+17	2.15E+10	1.25E+16	1.84E+02	6.85E+05	2.82E-27
67	40.00	7590	4.48E+14	4.25E+14	1.28E+17	8.63E+10	1.28E+16	2.66E+03	8.37E+06	2.18E-23
68	60.00	8220	1.05E+15	1.02E+15	1.30E+17	2.90E+11	1.31E+16	2.77E+04	7.39E+07	5.49E-20
69	80.00	8860	2.21E+15	2.18E+15	1.30E+17	8.23E+11	1.32E+16	2.12E+05	4.89E+08	4.96E-17
70	100.00	9400	3.87E+15	3.83E+15	1.31E+17	1.79E+12	1.35E+16	9.58E+05	1.99E+09	7.58E-15

TABLE 3

MODEL F

	Depth (km)	Temp. (K)	Electron	Proton	H(1)	H(2)	He(1)	He(2)	HeII	HeIII
			number density in (/cm**3)							
1	-2021.54	102770	1.88E+10	1.57E+10	3.27E+05	3.22E-01	2.53E+03	6.16E+00	6.20E+07	1.50E+09
2	-2021.02	98790	1.95E+10	1.63E+10	5.54E+05	5.37E-01	7.25E+03	1.64E+01	1.37E+08	1.49E+09
3	-2020.54	94800	2.02E+10	1.70E+10	8.10E+05	7.77E-01	1.76E+04	3.70E+01	2.26E+08	1.47E+09
4	-2020.09	90816	2.10E+10	1.78E+10	1.23E+06	1.17E+00	4.14E+04	8.03E+01	3.28E+08	1.45E+09
5	-2019.37	83891	2.26E+10	1.93E+10	2.88E+06	2.68E+00	1.59E+05	2.62E+02	5.58E+08	1.37E+09
6	-2018.66	75934	2.48E+10	2.14E+10	9.11E+06	8.34E+00	6.93E+05	9.28E+02	9.17E+08	1.22E+09
7	-2018.31	71336	2.62E+10	2.28E+10	1.92E+07	1.75E+01	1.64E+06	1.94E+03	1.16E+09	1.11E+09
8	-2017.94	66145	2.81E+10	2.46E+10	4.24E+07	3.90E+01	4.03E+06	3.86E+03	1.49E+09	9.72E+08
9	-2017.58	60170	3.06E+10	2.70E+10	9.54E+07	9.01E+01	9.98E+06	7.29E+03	1.87E+09	8.27E+08
10	-2017.21	53284	3.42E+10	3.04E+10	2.27E+08	2.29E+02	2.62E+07	1.29E+04	2.33E+09	6.96E+08
11	-2017.03	49385	3.67E+10	3.27E+10	3.59E+08	3.82E+02	4.35E+07	1.63E+04	2.59E+09	6.62E+08
12	-2016.86	45416	3.96E+10	3.54E+10	5.54E+08	6.31E+02	7.12E+07	1.94E+04	2.86E+09	6.50E+08
13	-2016.69	41178	4.33E+10	3.87E+10	8.59E+08	1.06E+03	1.18E+08	2.11E+04	3.17E+09	6.59E+08
14	-2016.52	36594	4.82E+10	4.32E+10	1.34E+09	1.82E+03	1.97E+08	1.99E+04	3.54E+09	7.02E+08
15	-2016.36	32145	5.42E+10	4.86E+10	2.03E+09	3.04E+03	3.23E+08	1.60E+04	3.96E+09	7.57E+08
16	-2016.21	27972	6.14E+10	5.51E+10	2.97E+09	4.84E+03	5.12E+08	1.08E+04	4.44E+09	8.42E+08
17	-2016.06	24056	7.01E+10	6.31E+10	4.30E+09	7.52E+03	7.76E+08	6.76E+03	5.03E+09	9.16E+08
18	-2015.90	20416	8.09E+10	7.31E+10	6.26E+09	1.15E+04	1.21E+09	5.42E+03	5.77E+09	9.37E+08
19	-2015.78	17925	9.03E+10	8.20E+10	8.16E+09	1.55E+04	1.79E+09	5.78E+03	6.34E+09	8.71E+08
20	-2015.66	15941	9.94E+10	9.09E+10	1.05E+10	2.02E+04	2.50E+09	6.88E+03	6.90E+09	7.03E+08
21	-2015.47	13897	1.10E+11	1.02E+11	1.49E+10	2.92E+04	3.79E+09	8.55E+03	7.46E+09	4.34E+08
22	-2015.26	12650	1.17E+11	1.09E+11	2.05E+10	4.09E+04	5.19E+09	9.62E+03	7.49E+09	2.46E+08
23	-2014.73	11650	1.18E+11	1.10E+11	3.49E+10	7.26E+04	7.61E+09	9.63E+03	6.79E+09	1.23E+08
24	-2014.00	11100	1.13E+11	1.06E+11	5.30E+10	1.14E+05	8.87E+09	1.03E+04	6.93E+09	8.44E+07
25	-2008.00	10500	1.10E+11	1.02E+11	7.47E+10	1.88E+05	9.85E+09	1.22E+04	7.71E+09	8.49E+07
26	-1995.00	10000	1.15E+11	1.07E+11	8.47E+10	2.12E+05	1.13E+10	1.32E+04	7.81E+09	7.77E+07
27	-1977.00	9700	1.19E+11	1.11E+11	9.81E+10	2.24E+05	1.30E+10	1.36E+04	7.77E+09	7.01E+07
28	-1955.00	9400	1.22E+11	1.14E+11	1.19E+11	2.37E+05	1.56E+10	1.35E+04	7.65E+09	6.09E+07
29	-1935.00	9200	1.24E+11	1.16E+11	1.39E+11	2.50E+05	1.83E+10	1.30E+04	7.18E+09	5.21E+07
30	-1923.00	9080	1.25E+11	1.17E+11	1.52E+11	2.57E+05	2.00E+10	1.25E+04	6.88E+09	4.68E+07
31	-1900.00	8900	1.27E+11	1.20E+11	1.79E+11	2.72E+05	2.37E+10	1.14E+04	6.15E+09	3.66E+07
32	-1880.00	8750	1.29E+11	1.23E+11	2.05E+11	2.85E+05	2.73E+10	1.02E+04	5.43E+09	2.84E+07
33	-1854.00	8550	1.31E+11	1.26E+11	2.45E+11	3.02E+05	3.26E+10	8.50E+03	4.46E+09	1.95E+07
34	-1818.00	8300	1.34E+11	1.30E+11	3.09E+11	3.25E+05	4.07E+10	6.31E+03	3.23E+09	1.08E+07
35	-1790.00	8100	1.37E+11	1.33E+11	3.71E+11	3.42E+05	4.80E+10	4.92E+03	2.46E+09	6.50E+06
36	-1760.00	7900	1.39E+11	1.37E+11	4.50E+11	3.60E+05	5.68E+10	3.76E+03	1.84E+09	3.91E+06
37	-1730.00	7750	1.43E+11	1.40E+11	5.39E+11	3.78E+05	6.66E+10	2.89E+03	1.39E+09	2.22E+06
38	-1680.00	7550	1.49E+11	1.46E+11	7.22E+11	4.08E+05	8.59E+10	1.97E+03	1.00E+09	1.17E+06
39	-1590.00	7340	1.59E+11	1.57E+11	1.19E+12	4.57E+05	1.35E+11	9.59E+02	4.28E+08	3.85E+05
40	-1475.00	7120	1.75E+11	1.72E+11	2.27E+12	5.29E+05	2.44E+11	5.45E+02	4.34E+08	1.77E+05
41	-1375.00	6930	1.90E+11	1.86E+11	4.04E+12	6.01E+05	4.22E+11	5.63E+02	6.42E+08	2.69E+04
42	-1275.00	6750	2.08E+11	2.03E+11	7.35E+12	6.93E+05	7.54E+11	6.81E+02	8.57E+08	2.15E+04
43	-1175.00	6550	2.24E+11	2.18E+11	1.38E+13	7.68E+05	1.40E+12	6.86E+02	8.64E+08	4.81E+03
44	-1075.00	6360	2.39E+11	2.32E+11	2.65E+13	8.45E+05	2.68E+12	1.69E+02	5.78E+07	3.87E+01
45	-975.00	6180	2.60E+11	2.49E+11	5.24E+13	9.52E+05	5.26E+12	1.20E+02	3.82E+07	8.52E+00
46	-900.00	6000	2.60E+11	2.43E+11	8.95E+13	9.17E+05	8.97E+12	9.38E+01	2.90E+07	2.81E+00
47	-850.00	5870	2.54E+11	2.31E+11	1.30E+14	8.56E+05	1.30E+13	8.00E+01	2.44E+07	1.33E+00
48	-800.00	5730	2.43E+11	2.12E+11	1.90E+14	7.62E+05	1.91E+13	6.87E+01	2.07E+07	5.88E-01
49	-750.00	5540	2.07E+11	1.63E+11	2.85E+14	5.50E+05	2.85E+13	6.09E+01	1.88E+07	2.73E-01
50	-700.00	5300	1.72E+11	1.09E+11	4.38E+14	3.20E+05	4.38E+13	4.71E+01	1.49E+07	9.65E-02
51	-650.00	5020	1.50E+11	5.58E+10	6.94E+14	1.49E+05	6.94E+13	3.21E+01	1.02E+07	2.43E-02
52	-600.00	4870	1.78E+11	3.54E+10	1.09E+15	1.16E+05	1.09E+14	1.89E+01	5.48E+06	3.00E-03
53	-550.00	4760	2.43E+11	2.36E+10	1.73E+15	1.08E+05	1.73E+14	9.62E+00	2.45E+06	2.17E-04
54	-525.00	4720	2.93E+11	2.00E+10	2.18E+15	1.12E+05	2.18E+14	5.78E+00	1.37E+06	4.45E-05
55	-500.00	4700	3.57E+11	1.85E+10	2.74E+15	1.28E+05	2.74E+14	2.98E+00	6.49E+05	7.21E-06
56	-450.00	4700	5.39E+11	1.92E+10	4.29E+15	2.01E+05	4.29E+14	4.12E-01	7.62E+04	6.23E-08
57	-400.00	4740	8.17E+11	2.46E+10	6.65E+15	3.85E+05	6.65E+14	1.73E-02	2.70E+03	5.12E-11
58	-350.00	4800	1.24E+12	3.54E+10	1.02E+16	8.07E+05	1.02E+15	1.22E-04	1.58E+01	1.16E-15
59	-300.00	4880	1.86E+12	5.74E+10	1.55E+16	1.83E+06	1.55E+15	1.52E-05	1.52E-01	3.03E-21
60	-250.00	4970	2.80E+12	1.01E+11	2.33E+16	4.26E+06	2.33E+15	5.33E-05	3.24E-01	4.72E-25
61	-200.00	5100	4.25E+12	2.24E+11	3.44E+16	1.15E+07	3.44E+15	2.56E-04	1.32E+00	4.38E-30
62	-150.00	5250	6.48E+12	5.64E+11	4.98E+16	3.23E+07	4.98E+15	1.40E-03	6.61E+00	2.37E-35
63	-100.00	5450	1.03E+13	1.72E+12	7.03E+16	1.04E+08	7.04E+15	1.02E-02	4.86E+01	1.14E-40
64	-50.00	5790	1.97E+13	7.53E+12	9.51E+16	5.05E+08	9.52E+15	1.65E-01	8.22E+02	2.13E-37
65	0.00	6520	7.67E+13	5.99E+13	1.18E+17	6.16E+09	1.18E+16	1.71E+01	7.31E+04	1.04E-30
66	20.00	6980	1.73E+14	1.53E+14	1.24E+17	2.15E+10	1.24E+16	1.83E+02	6.84E+05	2.83E-27
67	40.00	7590	4.47E+14	4.24E+14	1.27E+17	8.60E+10	1.28E+16	2.65E+03	8.35E+06	2.19E-23
68	60.00	8220	1.05E+15	1.02E+15	1.29E+17	2.89E+11	1.30E+16	2.76E+04	7.38E+07	5.49E-20
69	80.00	8860	2.21E+15	2.18E+15	1.30E+17	8.21E+11	1.32E+16	2.11E+05	4.88E+08	4.96E-17
70	100.00	9400	3.86E+15	3.82E+15	1.31E+17	1.78E+12	1.35E+16	9.55E+05	1.98E+09	7.58E-15

TABLE 4

MODEL P

	Depth (km)	Temp. (K)	Electron	Proton	H(1)	H(2)	He(1)	He(2)	HeII	HeIII
			number density in (/cm**3)							
1	-1741.97	121000	6.01E+10	5.02E+10	9.19E+05	2.98E+00	2.17E+03	1.17E+01	2.06E+08	4.81E+09
2	-1741.57	111000	6.59E+10	5.53E+10	1.42E+06	4.62E+00	1.09E+04	4.77E+01	5.27E+08	5.00E+09
3	-1741.22	101000	7.23E+10	6.11E+10	2.47E+06	7.98E+00	6.53E+04	2.21E+02	1.07E+09	5.04E+09
4	-1740.93	91000	7.99E+10	6.81E+10	6.70E+06	2.14E+01	4.18E+05	1.16E+03	1.94E+09	4.87E+09
5	-1740.68	81000	8.91E+10	7.70E+10	2.73E+07	8.60E+01	2.61E+06	5.60E+03	3.34E+09	4.40E+09
6	-1740.49	71000	1.01E+11	8.82E+10	1.19E+08	3.78E+02	1.29E+07	2.12E+04	5.18E+09	3.63E+09
7	-1740.33	61000	1.16E+11	1.03E+11	4.60E+08	1.55E+03	5.59E+07	5.97E+04	7.56E+09	2.71E+09
8	-1740.20	51000	1.36E+11	1.22E+11	1.50E+09	5.74E+03	2.05E+08	1.17E+05	1.02E+10	1.98E+09
9	-1740.15	46000	1.50E+11	1.35E+11	2.60E+09	1.09E+04	3.58E+08	1.40E+05	1.14E+10	1.99E+09
10	-1740.10	41000	1.67E+11	1.50E+11	4.29E+09	1.99E+04	6.39E+08	1.48E+05	1.27E+10	2.09E+09
11	-1740.05	36000	1.87E+11	1.68E+11	6.88E+09	3.55E+04	1.16E+09	1.33E+05	1.41E+10	2.23E+09
12	-1740.01	31000	2.14E+11	1.92E+11	1.08E+10	6.18E+04	1.89E+09	9.48E+04	1.55E+10	2.87E+09
13	-1739.96	26000	2.49E+11	2.25E+11	1.72E+10	1.07E+05	3.44E+09	5.07E+04	1.73E+10	3.39E+09
14	-1739.94	23500	2.73E+11	2.46E+11	2.17E+10	1.39E+05	4.20E+09	3.39E+04	1.84E+10	4.07E+09
15	-1739.91	21000	3.00E+11	2.71E+11	2.79E+10	1.83E+05	5.74E+09	2.62E+04	2.01E+10	4.12E+09
16	-1739.89	19000	3.27E+11	2.96E+11	3.45E+10	2.28E+05	7.64E+09	2.40E+04	2.09E+10	4.49E+09
17	-1739.86	17000	3.56E+11	3.26E+11	4.38E+10	2.88E+05	1.11E+10	2.61E+04	2.25E+10	3.50E+09
18	-1739.83	15000	3.91E+11	3.61E+11	5.74E+10	3.72E+05	1.54E+10	3.01E+04	2.39E+10	2.68E+09
19	-1739.78	13000	4.29E+11	4.04E+11	8.04E+10	5.09E+05	2.43E+10	3.58E+04	2.36E+10	5.17E+08
20	-1739.75	12000	4.51E+11	4.27E+11	1.00E+11	6.24E+05	3.04E+10	3.59E+04	2.19E+10	3.39E+08
21	-1739.72	11500	4.62E+11	4.42E+11	1.15E+11	7.12E+05	3.64E+10	3.46E+04	1.91E+10	2.32E+08
22	-1739.69	11000	4.73E+11	4.55E+11	1.36E+11	8.32E+05	4.21E+10	3.24E+04	1.68E+10	1.58E+08
23	-1739.65	10500	4.84E+11	4.69E+11	1.65E+11	9.91E+05	4.90E+10	2.96E+04	1.42E+10	1.15E+08
24	-1739.59	10000	4.86E+11	4.74E+11	2.08E+11	1.22E+06	5.67E+10	2.58E+04	1.14E+10	7.95E+07
25	-1739.55	9800	4.84E+11	4.72E+11	2.34E+11	1.35E+06	6.02E+10	2.44E+04	1.04E+10	6.91E+07
26	-1739.50	9600	4.79E+11	4.67E+11	2.67E+11	1.51E+06	6.30E+10	2.47E+04	1.02E+10	6.68E+07
27	-1739.43	9400	4.68E+11	4.56E+11	3.09E+11	1.69E+06	6.58E+10	2.60E+04	1.06E+10	6.90E+07
28	-1739.32	9200	4.50E+11	4.37E+11	3.66E+11	1.89E+06	6.93E+10	2.74E+04	1.10E+10	7.00E+07
29	-1739.25	9100	4.39E+11	4.26E+11	4.01E+11	2.00E+06	7.11E+10	2.90E+04	1.16E+10	7.39E+07
30	-1739.00	8900	4.07E+11	3.92E+11	4.87E+11	2.15E+06	7.45E+10	3.33E+04	1.33E+10	8.21E+07
31	-1738.50	8800	3.66E+11	3.49E+11	5.73E+11	2.08E+06	7.69E+10	3.74E+04	1.52E+10	8.87E+07
32	-1737.00	8700	3.36E+11	3.17E+11	6.43E+11	1.81E+06	7.97E+10	3.96E+04	1.64E+10	9.01E+07
33	-1734.50	8600	3.17E+11	2.98E+11	6.97E+11	1.59E+06	8.32E+10	3.91E+04	1.63E+10	8.79E+07
34	-1723.00	8500	2.98E+11	2.84E+11	7.83E+11	1.45E+06	9.53E+10	2.68E+04	1.14E+10	5.73E+07
35	-1700.00	8400	3.09E+11	3.03E+11	8.77E+11	1.53E+06	1.13E+11	1.10E+04	4.60E+09	1.94E+07
36	-1660.00	8250	3.44E+11	3.40E+11	1.06E+12	1.73E+06	1.38E+11	3.45E+03	1.66E+09	4.51E+06
37	-1575.03	8000	4.11E+11	4.08E+11	1.65E+12	2.08E+06	2.05E+11	1.10E+03	8.99E+08	2.47E+05
38	-1475.03	7700	4.57E+11	4.53E+11	2.91E+12	2.27E+06	3.36E+11	4.19E+02	3.92E+08	9.67E+03
39	-1380.00	7420	4.79E+11	4.74E+11	5.03E+12	2.35E+06	5.50E+11	2.55E+02	2.23E+08	2.14E+03
40	-1280.00	7150	4.84E+11	4.78E+11	9.06E+12	2.33E+06	9.54E+11	1.76E+02	1.18E+08	3.66E+02
41	-1210.00	6980	4.91E+11	4.83E+11	1.39E+13	2.36E+06	1.44E+12	1.60E+02	1.05E+08	2.02E+02
42	-1065.00	6600	4.85E+11	4.74E+11	3.54E+13	2.31E+06	3.58E+12	9.88E+01	4.49E+07	1.26E+01
43	-980.00	6390	4.73E+11	4.58E+11	6.35E+13	2.22E+06	6.39E+12	8.48E+01	1.86E+07	1.71E+00
44	-905.00	6220	4.75E+11	4.53E+11	1.07E+14	2.24E+06	1.08E+13	5.70E+01	1.39E+07	5.47E-01
45	-855.00	6090	4.64E+11	4.35E+11	1.54E+14	2.14E+06	1.55E+13	4.45E+01	1.16E+07	2.48E-01
46	-750.00	5740	3.84E+11	3.30E+11	3.44E+14	1.44E+06	3.44E+13	2.87E+01	7.66E+06	3.63E-02
47	-700.00	5480	3.02E+11	2.24E+11	5.24E+14	8.22E+05	5.24E+13	2.19E+01	6.08E+06	1.34E-02
48	-650.00	5220	2.50E+11	1.36E+11	8.15E+14	4.37E+05	8.15E+13	1.65E+01	4.64E+06	3.91E-03
49	-600.00	5070	2.67E+11	9.83E+10	1.26E+15	3.48E+05	1.26E+14	1.12E+01	2.97E+06	6.18E-04
50	-550.00	4960	3.27E+11	7.39E+10	1.95E+15	3.28E+05	1.95E+14	5.60E+00	1.35E+06	5.09E-05
51	-500.00	4910	4.48E+11	6.57E+10	3.00E+15	4.02E+05	3.00E+14	1.51E+00	3.24E+05	1.62E-06
52	-450.00	4900	6.44E+11	6.78E+10	4.59E+15	5.94E+05	4.59E+14	1.77E-01	3.30E+04	1.09E-08
53	-400.00	4940	9.51E+11	8.73E+10	6.96E+15	1.10E+06	6.96E+14	6.08E-03	9.70E+02	6.33E-12
54	-350.00	5000	1.41E+12	1.24E+11	1.04E+16	2.20E+06	1.05E+15	7.21E-05	5.23E+00	1.13E-16
55	-300.00	5070	2.10E+12	1.87E+11	1.56E+16	4.55E+06	1.56E+15	1.01E-04	9.38E-01	6.40E-21
56	-250.00	5170	3.13E+12	3.26E+11	2.30E+16	1.05E+07	2.30E+15	3.41E-04	2.52E+00	1.01E-24
57	-200.00	5280	4.70E+12	6.10E+11	3.34E+16	2.46E+07	3.34E+15	1.24E-03	7.63E+00	7.55E-30
58	-150.00	5400	7.11E+12	1.21E+12	4.80E+16	5.83E+07	4.80E+15	4.77E-03	2.61E+01	2.99E-35
59	-100.00	5550	1.11E+13	2.69E+12	6.80E+16	1.49E+08	6.80E+15	2.16E-02	1.12E+02	4.90E-40
60	-50.00	5880	2.20E+13	1.00E+13	9.20E+16	6.68E+08	9.20E+15	2.93E-01	1.49E+03	1.80E-36
61	0.00	6520	7.58E+13	5.94E+13	1.15E+17	6.03E+09	1.15E+16	1.67E+01	7.30E+04	1.06E-30
62	20.00	6980	1.71E+14	1.52E+14	1.21E+17	2.10E+10	1.21E+16	1.79E+02	6.78E+05	2.84E-27
63	40.00	7590	4.42E+14	4.19E+14	1.24E+17	8.41E+10	1.25E+16	2.59E+03	8.26E+06	2.18E-23
64	60.00	8220	1.04E+15	1.01E+15	1.26E+17	2.82E+11	1.27E+16	2.70E+04	7.30E+07	5.49E-20
65	80.00	8860	2.19E+15	2.15E+15	1.27E+17	8.02E+11	1.29E+16	2.06E+05	4.83E+08	4.96E-17
66	100.00	9400	3.82E+15	3.78E+15	1.28E+17	1.74E+12	1.32E+16	9.34E+05	1.96E+09	7.58E-15

where $\nabla \equiv d/dz$ in the present one-dimensional case. Here $F_{\rm H}$ and $F_{\rm He}$ are the particle fluxes expressed in terms of the "mass velocity" U (see Paper I) and the diffusion velocities according to

$$\begin{aligned} F_{\rm H} &= n_{\rm H}(V_{\rm H} + U) \\ &= (n_p V_p + n_a V_a) + n_{\rm H} U, \\ F_{\rm He} &= n_{\rm He}(V_{\rm He} + U) \\ &= (n_{\rm I} V_{\rm I} + n_{\rm II} V_{\rm II} + n_{\rm III} V_{\rm III}) + n_{\rm He} U . \end{aligned} \tag{7}$$

These equations provide definitions of $V_{\rm H}$ and $V_{\rm He}$, the total diffusion velocities of hydrogen and helium in all ionization stages. In the stationary one-dimensional case, $F_{\rm H}$ and $F_{\rm He}$ are both constant.

We now multiply equations (6), and the corresponding equation for electrons, by the hydrogen, helium, and electron masses, respectively, to obtain the mass conservation equation

$$\frac{\partial \rho}{\partial t} + \nabla \cdot M_m = \frac{\partial (m_{\rm H} n_{\rm H} + m_{\rm He} n_{\rm He} + m_e n_e)}{\partial t} + \nabla \cdot (m_{\rm H} F_{\rm H} + m_{\rm He} F_{\rm He} + m_e F_e) = 0 , \tag{8}$$

where M_m is the mass flow. In the stationary one-dimensional case M_m is a constant. In the fluid frame (i.e., moving with velocity U) the mass flow must vanish (because of the definition of this frame), so that

$$m_{\rm H} n_{\rm H} V_{\rm H} + m_{\rm He} n_{\rm He} V_{\rm He} + m_e n_e V_e = 0 , \tag{9}$$

which is a relation that the diffusion velocities satisfy (in the way in which they are defined here). Consequently, the mass flow is given by

$$M_m = \rho U = (m_{\rm H} n_{\rm H} + m_{\rm He} n_{\rm He} + m_e n_e) U , \tag{10}$$

which is the usual mass conservation equation. In most cases the electron mass and flow terms can be neglected in this mass transfer equation (but not, of course, in the equations for electric charge and energy transport, as will be shown later).

We now define the useful parameter N_m, which describes the total mass flow of hydrogen relative to helium,

$$N_m = m_{\rm H} F_{\rm H} - m_{\rm He} F_{\rm He} , \tag{11}$$

or, in terms of M_m,

$$N_m = (m_{\rm H} n_{\rm H} V_{\rm H} - m_{\rm He} n_{\rm He} V_{\rm He}) + (m_{\rm H} n_{\rm H} - m_{\rm He} n_{\rm He})(M_m/\rho) . \tag{12}$$

From equations (6) it follows that

$$\frac{\partial}{\partial t}(m_{\rm H} n_{\rm H} - m_{\rm He} n_{\rm He}) + \nabla \cdot N_m = 0 , \tag{13}$$

which shows that N_m is also a constant in stationary one-dimensional cases.

The two quantities M_m and N_m (constants in stationary, one-dimensional cases) can be redefined for convenience by dividing by the hydrogen atom mass: $M = (M_m/m_{\rm H})$ and $N = (N_m/m_{\rm H})$. Equation (9) restricts the possible values of the number densities and diffusion velocities, and the restriction corresponds to the fact that these velocities are defined in the fluid frame. Consequently, the set of diffusion velocities V_e, V_p, V_a, $V_{\rm I}$, $V_{\rm II}$, $V_{\rm III}$ is not independent (see Paper I), and these velocities can be expressed in terms of a smaller set of relative diffusion velocities. We define this set as

$$\begin{aligned} V_A &= V_a - V_p , \\ V_B &= V_{\rm H} - V_{\rm He} \\ &= (n_p V_p + n_a V_a) - (n_{\rm I} V_{\rm I} + n_{\rm II} V_{\rm II} + n_{\rm III} V_{\rm III}) , \\ V_C &= V_{\rm I} - V_{\rm II} , \\ V_D &= V_{\rm II} - V_{\rm III} , \\ V_E &= (n_p V_p + n_{\rm II} V_{\rm II} + 2 n_{\rm III} V_{\rm III})/n_e - V_e , \end{aligned} \tag{14}$$

where the last equation corresponds to the electric current divided by the proton charge. In our present calculations we will assume that the electric current vanishes (thus defining V_e in terms of V_p, $V_{\rm II}$, and $V_{\rm III}$) because otherwise a "space charge" will build up such that the resulting electric field will stop the current flow (see Paper I). This zero-current electric field due to space charge in the plasma (i.e., small departure from neutrality) generally has some effects on the diffusion, as we will show later. The equilibrium electric field is accounted for (implicitly) in our transport theory. Here we neglect any externally imposed electric field which may also be present. When an external field, $E_{\rm ext}$, is added to this zero-current self-consistent field, E_0, electric currents arise according to the modified form of Ohm's law (e.g., see Spitzer 1962).

Using the transport theory summarized in the Appendix, we express the relative diffusion velocities as linear functions of the following logarithmic gradients of the number density ratios and the temperature (the pressure gradient effects are neglected):

$$\begin{aligned} Z_A &= \nabla \ln (n_p/n_a) , \\ Z_B &= \nabla \ln (n_{\rm He}/n_{\rm H}) , \\ Z_C &= \nabla \ln (n_{\rm II}/n_{\rm I}) , \\ Z_D &= \nabla \ln (n_{\rm III}/n_{\rm II}) , \\ Z_T &= \nabla \ln T . \end{aligned} \tag{15}$$

The transport theory summarized in the Appendix gives linear expressions for all the relative diffusion velocities

$$\begin{aligned} V_A &= d_{11} Z_A + d_{12} Z_B + d_{13} Z_C + d_{14} Z_D + d_{15} Z_T , \\ V_B &= d_{21} Z_A + d_{22} Z_B + d_{23} Z_C + d_{24} Z_D + d_{25} Z_T , \\ V_C &= d_{31} Z_A + d_{32} Z_B + d_{33} Z_C + d_{34} Z_D + d_{35} Z_T , \\ V_D &= d_{41} Z_A + d_{42} Z_B + d_{43} Z_C + d_{44} Z_D + d_{45} Z_T . \end{aligned} \tag{16}$$

An additional equation may be included if one wishes to consider electric current (V_E different from zero), and other terms must be added to equations (16) for an external electric field.

Equations (14) can be solved to express V_a, V_p, $V_{\rm I}$, $V_{\rm II}$, and $V_{\rm III}$ in terms of V_A, V_B, V_C, and V_D. The result is

$$\begin{aligned} V_a &= \frac{n_p}{n_{\rm H}} V_A + \frac{ba}{1+ba} V_B , \\ V_p &= -\frac{n_a}{n_{\rm H}} V_A + \frac{ba}{1+ba} V_B , \\ V_{\rm I} &= -\frac{1}{1+ba} V_B + \frac{n_{\rm II} + n_{\rm III}}{n_{\rm He}} V_C + \frac{n_{\rm III}}{n_{\rm He}} V_D , \\ V_{\rm II} &= -\frac{1}{1+ba} V_B - \frac{n_{\rm I}}{n_{\rm He}} V_C + \frac{n_{\rm III}}{n_{\rm He}} V_D , \\ V_{\rm III} &= -\frac{1}{1+ba} V_B - \frac{n_{\rm I}}{n_{\rm He}} V_C - \frac{n_{\rm I} + n_{\rm II}}{n_{\rm He}} V_D , \end{aligned} \tag{17}$$

where $a = n_{He}/n_H$ is the helium-to-hydrogen abundance ratio and $b = m_{He}/m_H$. Note that the first term in the first two equations is the same as for hydrogen diffusion derived in our Papers I and II, but now there is an added term proportional to $V_H - V_{He}$. (Note that this term goes to zero if the He abundance is zero.)

So far, we have only considered the main species present in the gas, namely, electrons, protons, hydrogen atoms, and neutral, singly ionized, and doubly ionized helium. However, the atoms and singly ionized helium contain many bound energy levels, for which we solve the equations of statistical equilibrium. Here we assume that all energy states of a given species share the common diffusion velocity specified above. This is a good assumption because the transition rates between levels are fast enough to ensure the close coupling of the particle momentum between energy levels. The most critical case may be that of the helium triplet levels. However, the transition rate (mostly collisional) between triplet and singlet levels is fast enough for all the cases we consider here. (This may not be true in the case of very low density material with a steep temperature gradient.)

We use the following statistical equilibrium equations for each bound energy level with index m

$$\frac{\partial n_m}{\partial t} + \nabla \cdot [n_m(V_m + U)] = R_m , \tag{18}$$

where R_m is the net rate of transitions (radiative and collisional) into level m from all other levels and continua. Also, V_m in equation (18) is the diffusion velocity corresponding to n_m (V_a for hydrogen levels, V_p for protons, V_I for He I, V_{II} for He II, and V_{III} for He III). For the bound levels of hydrogen and neutral helium,

$$R_m = \sum_{n \neq m} n_n P_{nm} + n_\kappa P_{\kappa m} - n_m\left(\sum_{n \neq m} P_{mn} + P_{m\kappa}\right), \tag{19}$$

where P_{nm} is the rate coefficient for transitions from level n to level m, and the index κ refers to the continuum. When we consider the bound levels of He II and its continuum (He III), we must also take into account the transitions between the ground level of He II and all He I levels. (We neglect transitions between He I and the excited He II levels and between He I and He III.) These He II to He I transition rates are computed as part of the He I calculation. The term R_m for level 1 of He II then becomes

$$R_1 = \sum_{l>1} n_l P_{l1} + n_\kappa P_{\kappa 1} - n_1\left(\sum_{l>1} P_{1l} + P_{1\kappa}\right) - \sum_q (n_1 P_{1q} - n_q P_{q1}) , \tag{20}$$

where l refers to the remaining bound levels of He II, κ to He III, and q to the bound levels of He I. The R_m term given by equation (19) is used for the He II levels $m > 1$, and for all He I levels.

Equations (18)–(20) are sufficient to compute the level populations, provided that the rate coefficients and the terms on the left are known. These left-side terms principally affect the statistical equilibrium equations for ionization, giving important departures from the solution for static cases without diffusion (i.e., local ionization). A possible procedure is to evaluate the left-hand side from available number densities, solve the set of statistical equilibrium equations for the number densities, re-evaluate each left-hand side and repeat this over and over. This procedure generally does not converge because it does not properly account for the differential character of the left-hand side, which links the solution at one depth with that at neighboring depths. The level 1 number densities for H, He I, and He II must be determined by solving equation (18) as a differential equation for n_1 as a function of depth. (The equations for levels $m > 1$ can be solved by iteration.) Using equations (15)–(17) to express the diffusion velocities in terms of the number densities, we derive a second-order differential expression for the level 1 number density of H, He I, and He II having the form

$$\frac{d}{dz}\left(g n_1 - f \frac{dn_1}{dz}\right) + n_1 r = s . \tag{21}$$

Here f is given by d_{11} for H, and by d_{33} for He I (see eq. [16]). In the case of He II, $f = f_1 + f_2$, where

$$f_1 = \frac{n_I + n_{II}}{n_{He}} d_{33} , \quad f_2 = \frac{n_{II} + n_{III}}{n_{He}} d_{44} . \tag{22}$$

The values of g are given by

$$\begin{aligned} g &= f \frac{d \ln (n_a + 2n_p)}{dz} + \frac{n_p}{n_H} \Delta_a + \frac{ab V_B}{1 + ab} + U , \\ g &= f \frac{d \ln (n_{He})}{dz} + (d_{44} - d_{33}) \frac{n_{II}}{n_{He}} Z_D \\ &\quad + \frac{n_I + n_{II}}{n_{He}} \Delta_1 + \frac{n_{II}}{n_{He}} \Delta_2 - \frac{V_B}{1 + ab} + U , \\ g &= f_1 \frac{d \ln (n_I + n_{II})}{dz} + f_2 \frac{d \ln (n_{II} + n_{III})}{dz} \\ &\quad - \frac{n_I}{n_{He}} \Delta_1 + \frac{n_{III}}{n_{He}} \Delta_2 - \frac{V_B}{1 + ab} + U , \end{aligned} \tag{23}$$

for H, He I, and He II, respectively, where

$$\begin{aligned} \Delta_a &= d_{12} Z_B + d_{13} Z_C + d_{14} Z_D + d_{15} Z_T , \\ \Delta_1 &= d_{31} Z_A + d_{32} Z_B + d_{34} Z_D + d_{35} Z_T , \\ \Delta_2 &= d_{41} Z_A + d_{42} Z_B + d_{43} Z_C + d_{45} Z_T . \end{aligned} \tag{24}$$

The term r in equation (21) is given by

$$r = P_{1\kappa} + \sum_{n>1} (n_n/n_1)(P_{n\kappa} + G_n) , \tag{25}$$

with

$$G_n = \frac{1}{n_n}\left\{\frac{\partial n_n}{\partial t} + \nabla \cdot [n_n(V_n + U)]\right\}, \tag{26}$$

and the s term in equation (21) is

$$s = n_\kappa \sum_n P_{\kappa n} \tag{27}$$

for H and He I, and

$$s = n_\kappa \sum_n P_{\kappa n} - \left\{\frac{\partial n_I}{\partial t} + \nabla \cdot [n_I(V_I + U)]\right\} \tag{28}$$

for He II.

Equations (21) for the level 1 number densities of H, He I, and He II are solved numerically for $n_1(z)$ using coefficients f, g, r, and s computed from the number densities determined in the previous iteration. Then all the number densities are rescaled

and recomputed by solving equations (18)–(20) together with the radiative transfer equations, but now with the left-hand sides of equations (18) fixed. We find that this scheme converges to self-consistent values which satisfy all the basic equations. We have adopted this procedure to be able to use our existing method of solving the coupled equations of radiative transfer and statistical equilibrium, by combining the given terms on the left with given rate coefficients on the right. Other procedures could be devised to simultaneously solve the entire system of equations.

4. THE ENERGY-BALANCE MODELS

We have constructed four models, A, C, F, and P. The first three models correspond to components of the quiet Sun: a faint cell center area (A), an average intensity area (C), and a bright area of the network (F). Model P corresponds to a plage area of medium brightness. The quiet-Sun models of the photosphere and chromosphere are those of VAL, as modified by Avrett (1985) in the temperature mimimum region, and by Maltby et al. (1986) in the photosphere. The plage model photosphere and chromosphere is based on a modification of the model by Lemaire et al. (1981). In the present paper we compute energy-balance models of the low transition regions for these four models. Our transition-region models include hydrogen and helium diffusion, satisfy the statistical equilibrium equations (18)–(23), and correspond to energy balance between inflowing particle heat flux and outflowing net radiative flux. The energy balance is not determined in this way in the chromospheric and photospheric layers where the temperature structure is taken from previous models based on observations. Thus, local nonradiative heating other than particle heat flux plays the major role in supplying energy to these lower layers. Diffusion is considered throughout the models, but it is not important except in the transition region. We have included "microturbulent" velocities in the equation of hydrostatic equilibrium (eq. [1]) in the form of a turbulent contribution to the pressure, as described by VAL, and we determine the turbulent velocity as specified in Paper II. The calculations are based on the equations in the preceding section and those in Papers I and II. Our present hydrostatic models assume zero-mass velocity U, i.e., $M = 0$. Here we assume that the helium-to-hydrogen abundance ratio a is constant through the atmosphere and has the value 0.1. In a later section we will consider the abundance changes which ambipolar diffusion would produce, and we comment on the effects of mass flows in moderating these changes. In this paper we consider only the classical diffusion which arises from the nonzero mean free paths of electrons and heavy particles between collisions, and we do not include ad hoc macroscopic velocity effects such as considered by Cally (1990), Woods & Holzer (1991), and Athay (1990). The effects considered here are the results of well-understood physics, and need to be accounted for in any case. Our results should be interpreted as a lower limit on the diffusion processes because diffusion may be increased somewhat by small-scale hydrodynamic turbulence in nonhydrostatic cases.

The model temperature distributions are shown in Figure 3 and listed in Tables 1–4 for reference. However, the transition region is so narrow that it is essentially a vertical line in Figure 3. For this reason we show in Figure 4 the transition regions in a different form. The quantity plotted as function of temperature in Figure 4 is the standard emission measure

$$\mathrm{SEM} = n_e n_{\mathrm{H}} (d \ln T/dz)^{-1} \qquad (29)$$

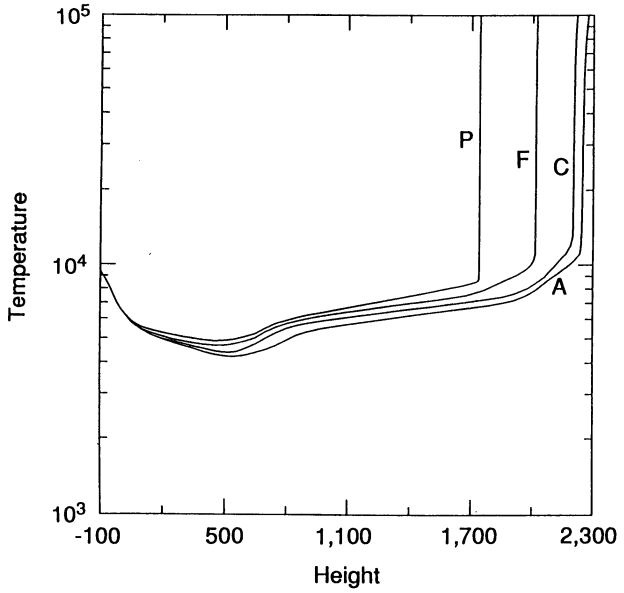

FIG. 3.—Temperature structure of our models A, C, F, and P. The height is measured in kilometers from the level; the temperature is in kelvins.

in units of cm^{-5}. The curves plotted in Figure 4 do not differ qualitatively from those obtained from the usual analyses of line intensities. However, the semiempirical studies use local statistical equilibrium to determine neutral and ion number densities, whereas in our nonlocal calculations the neutral atom number densities are much larger at high temperatures, and the ion number densities much larger at low temperatures, than in local ionization equilibrium. Figure 5 shows the neutral hydrogen and proton number densities that we compute for model C plotted against height compared with the

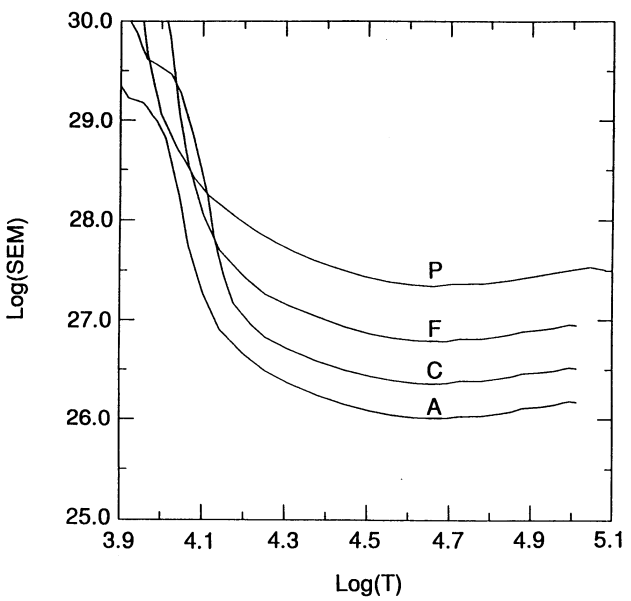

FIG. 4.—"Standard emission measure" (cm^{-5}) for our models A, C, F, and P, as a function of temperature (K). These graphs show the variations of the structure of the low transition region and permit comparisons with other models.

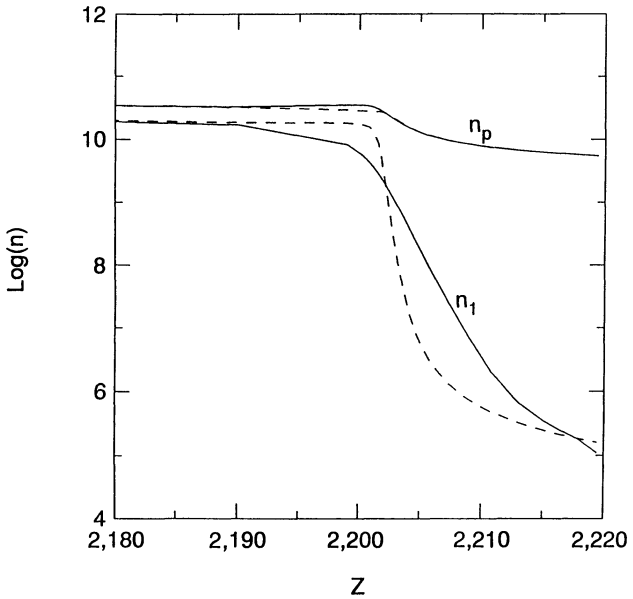

FIG. 5.—Effects of diffusion on the neutral hydrogen (ground level) and proton number densities (cm^{-3}) for model C. The solid line shows the results of our calculation including diffusion, and the dashed line shows the results assuming local statistical equilibrium, ignoring diffusion. Both calculations correspond to the same values of temperature as a function of height.

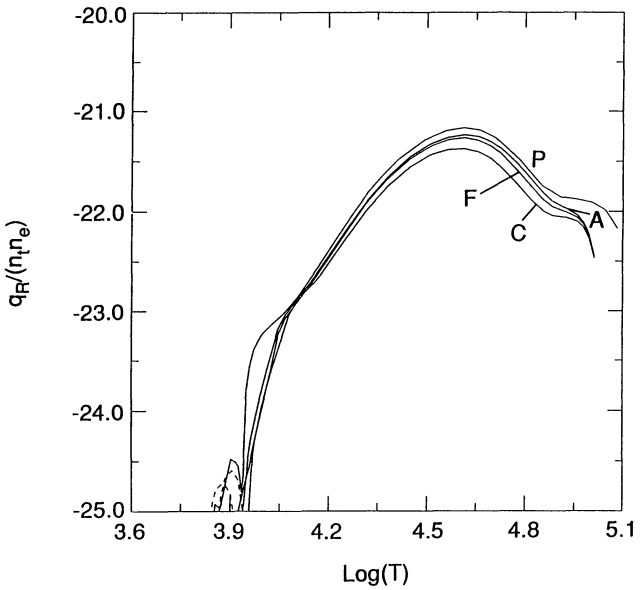

FIG. 7.—Total radiative loss function (ergs cm^3 s^{-1}) for H and He combined for our models A, C, F, and P. The solid line corresponds to positive values and the dashed line to negative radiative losses.

corresponding values computed for the same $T(z)$ in the same way except without diffusion. Figure 6 shows the corresponding results for He I, He II, and He III.

Figure 7 shows the values of the total radiative losses for H and He combined, divided by the electron and the total hydrogen densities, as a function of the temperature in our models. Because the temperature is monotonically increasing, we can map the height to temperature in each model and plot all the curves in a common scale. This figure is intended to show that there is practically a common curve which describes these radiative losses between 14,000 and 80,000 K. The losses in this range are strongly dominated by the Lyα line. However, outside this temperature range the losses (per electron and hydrogen nucleus) start to depart significantly from a common curve. The departures are not very large for the quiet-Sun models at temperatures above 10,000 K. But the plage model (model P) has significantly increased values between 10,000 and 14,000 K. This may seem strange in view of what is only a moderate increase in the hydrogen emission intensities (relative to the bright-network model F; see below). The reason for the increased values is the increased importance of the losses in the Lyman continuum, which become a significant fraction of the total losses at this temperature for model P. The radiative losses increase more than those given by the optically thin formulation because of lower departures from LTE. Below some temperature in the range between 8000 and 9000 K, the radiative losses decrease to negative values, so that backwarming occurs (see Papers I and II). These negative radiative losses by hydrogen and helium are assumed to be compensated by other emissions, the prime candidates being the strong emission cores of the *h* and *k* lines of Mg II. Another significant departure between the curves arises above 80,000 K, and this is due to an increase and shift to higher temperatures of the He II emission (basically the 304 Å line). In Figure 8*a* we show the He I radiative losses, and in Figure 8*b* we compare the He II radiative losses with the total losses (for H and He) from Figure 7. The three figures show that the He I losses are everywhere negligible compared with those of hydrogen, but the He II losses become dominant for temperatures above 70,000 K. Figures 8*a* and 8*b* also show that there is backwarming for He I but not for He II. It is clear in Figure 8*b* that the He II curves for the four models have a similar shape, but they overlap only between 40,000 and 80,000 K. (For the quiet-Sun models A, C, and F, the overlap extends up to 100,000 K.) This indicates

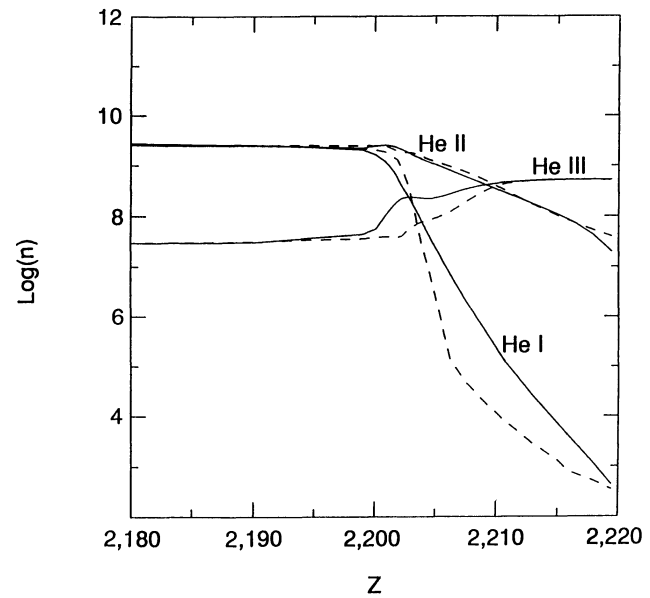

FIG. 6.—Effects of diffusion on neutral and singly and doubly ionized helium. The solid line shows the results of our calculation including diffusion, and the dashed line shows the results ignoring diffusion. Both calculations correspond to the same values of temperature as a function of height. The He II number density decreases relative to He I at smaller heights.

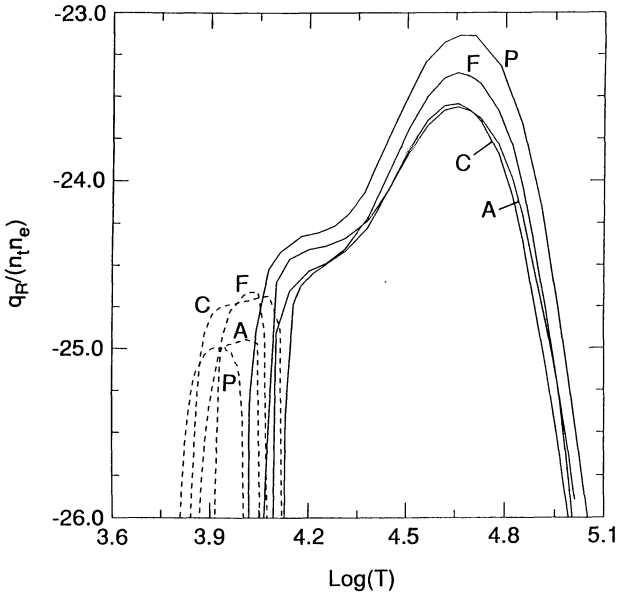

FIG. 8a

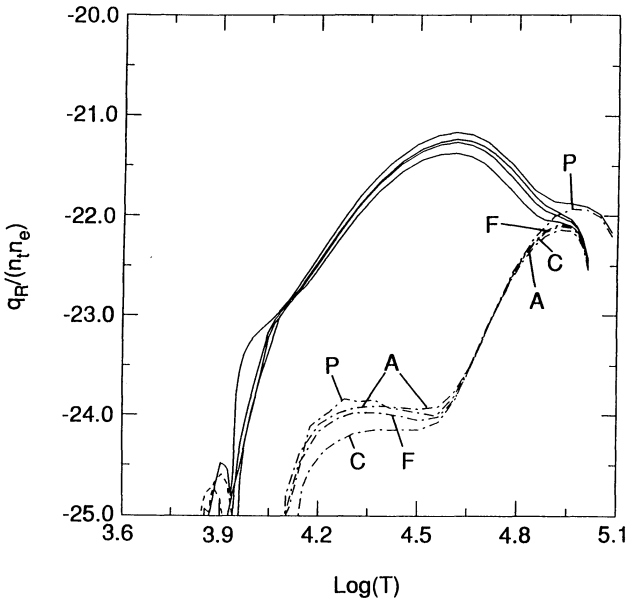

FIG. 8b

FIG. 8.—(*a*) He I radiative loss function for models A, C, F, and P. The solid line corresponds to positive values and the dashed line to negative values of the radiative losses. (*b*) He II radiative loss function for models A, C, F, and P (*dash-dot lines*) compared with the total H and He radiative loss from Fig. 7.

that there are departures from the optically thin expression

$$q_R = \Phi(T) n_e n_H \,. \tag{30}$$

However, the magnitude of these departures is not large (in view of the large density variations between our models) and consequently equation (30) can be used to estimate the total losses (provided that the appropriate temperatures of formation are used; see Paper II). One of the most significant departures from this formula arises for He II in model P. A numerical approximation to the radiative losses for the temperature range between 10,000 and 100,000 K is given by a fit to our plots of Figure 7,

$$\log_{10} \Phi = -146.27 + 54.13X - 5.864X^2 \,, \tag{31}$$

where $X = \log_{10} T$ and where Φ is in ergs cm^3 s^{-1}. Comparing the He radiative losses with the values from Cox & Tucker (1969, hereafter CT) we find that our computations for He II reach a similar peak at about 90,000 K but our curves for models A, C, and F indicate larger losses at lower temperatures (e.g., the losses decrease by only about a factor of 10 at 50,000 K). The curve for model P indicates that, for a plage, losses larger than the CT values occur up to 120,000 K. The radiative losses for He I are also different from the CT values and display large changes from one model to another, especially between models F and P. Particularly noticeable are the negative values of the He I radiative losses in the temperature range between 6500 and 14,000 K. This indicates that an optically thin expression such as

$$I_{\text{thin}} = n_e n_H \alpha_{\text{thin}}(T) \tag{32}$$

is not accurate for describing the He I line intensities.

Another important quantity in our models is the ambipolar diffusion velocity. In Figure 9 we plot this velocity for our current models, again as a function of the temperature. From these curves and the proton and neutral hydrogen number densities one can obtain the atom (upward) and proton (downward) diffusion velocities shown in Paper I. We note that all curves in Figure 9 nearly overlap for temperatures from 14,000 K up to the highest values in our calculations (about 100,000 K). The differences below 14,000 K occur because the temperature distribution is required to join smoothly with the chromospheric temperatures, and no energy balance was computed. We have imposed no a priori behavior on the calculated diffusion velocity, and it is remarkable that our energy-balance calculations including energy transport by diffusion and nonlocal hydrogen ionization produce temperature and ionization gradients such that the ambipolar velocity becomes essentially

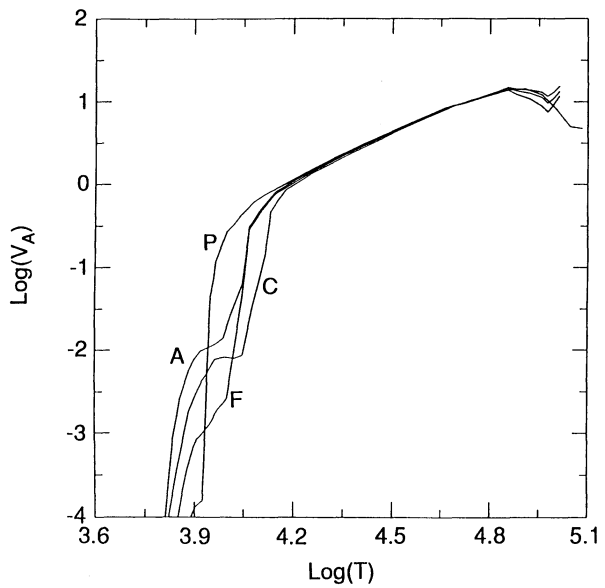

FIG. 9.—Hydrogen-to-proton relative diffusion velocity, V_A (km s^{-1}), for models A, C, F, and P. This velocity is nearly equal to the ambipolar diffusion velocity, but there is a small difference due to the presence of helium ions. The H-to-He relative diffusion velocity, V_B, is assumed to be zero.

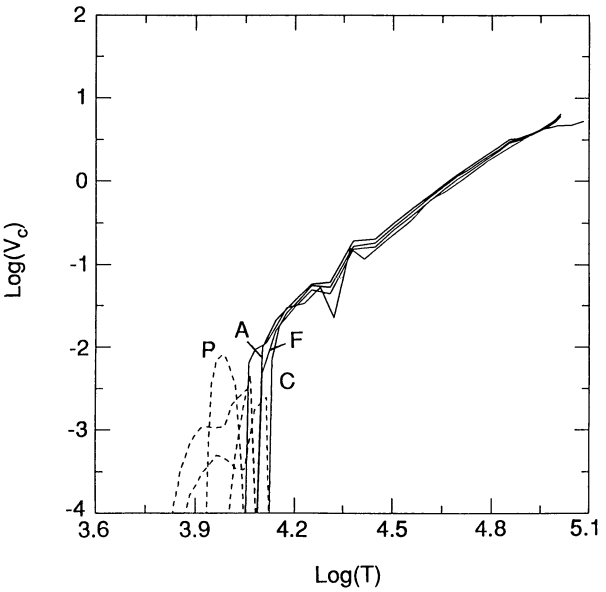

FIG. 10.—He I–to–He II relative diffusion velocity, V_C (km s^{-1}), for models A, C, F, and P. The solid line corresponds to positive (outward) velocities, and the dashed line corresponds to negative velocities. These negative values arise due to an outflow of He II relative to He I.

model-independent. A numerical fit to the plot for the ambipolar velocity in the range between 14,000 and 100,000 K is

$$\log_{10} V_A = -44.01 + 20.36X - 2.07X^2 , \quad (33)$$

where $X = \log_{10} T$ and V_A is in centimeters per second.

Figures 10 and 11 show the relative helium diffusion velocities V_C and V_D defined in equations (14). The diffusion velocity of helium relative to hydrogen, V_B, is irrelevant here because we have assumed a constant helium abundance. We note that again the diffusion velocities become more or less model-independent in the temperature range where the energy balance is computed (although V_D is more model-dependent).

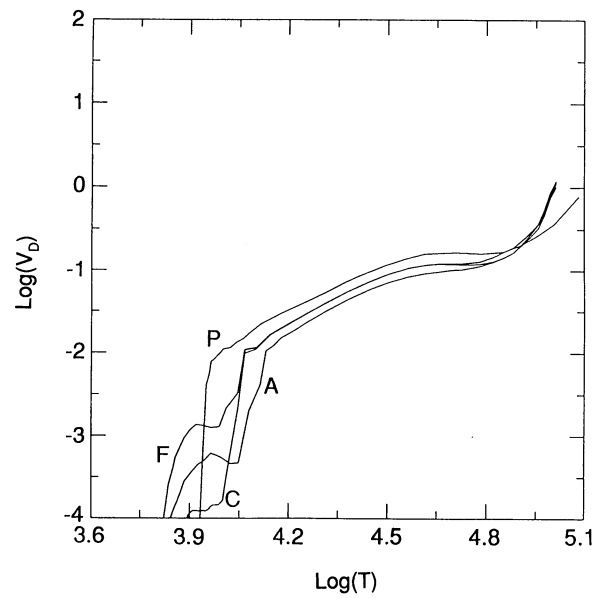

FIG. 11.—He II–to–He III relative diffusion velocity, V_D (km s^{-1}), for models A, C, F, and P.

The effects of the diffusion shown in detail for model C in Figures 5 and 6 are present in all our models. The main effect is the smoothing of the ionization state changes over a short distance between neutral and ionized regions. The effect on the transition between helium ionization stages is more complicated than that of hydrogen because of the presence of residual He I at high temperatures and residual He III at low temperatures.

The helium ionization energy transported by helium diffusion was included in our calculations of total heat flux in the same way as was described for an arbitrary gas mixture in the Appendix of Paper I. We find that this contribution to the heat flux is not very important. But the energy losses by He II dominate at temperatures of about 80,000 K. These losses affect the temperature stratification in our energy-balance calculations by maintaining the steep temperature gradient at temperatures close to 100,000 K.

5. EMITTED INTENSITIES AND PROFILES

The computed UV resonance line intensities from our models are shown in Figures 12–15. The 304 Å He II resonance line (Fig. 12) shows a simple emission line with no reversal, but the flat top indicates that substantial self-absorption effects appear in all models. The full width at half-maximum (FWHM) is about 0.07 Å for all the models. This computed width can be compared to the observed width of about 0.10 Å reported by Cushman & Rense (1978), who also noted that the top of the line seemed flatter than a Gaussian profile. The calculated 304 Å integrated intensities in Table 5 can be compared to their observed value of about 7000 ergs cm^{-2} s^{-1} sr^{-1}. Other observed values range between 2280 and 10,500 ergs cm^{-2} s^{-1} sr^{-1} (Mango et al. 1978; Linsky et al. 1976). Our calculated values 440 (A), 920 (C), 2700 (F), and 15,000 (P) are generally smaller than these observations, but, as noted below, the spatially averaged observations should correspond to larger computed intensities than those of model C.

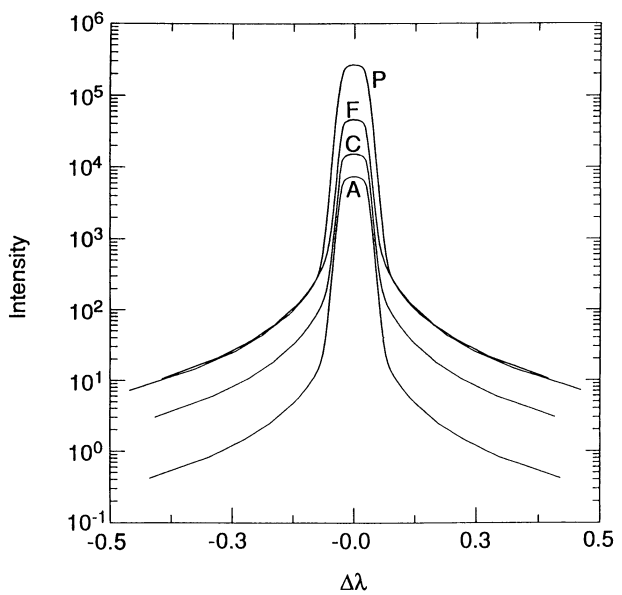

FIG. 12.—He II 304 Å line profile for models A, C, F, and P. Here and in subsequent figures, the intensity is in ergs cm^{-2} s^{-1} sr^{-1} Å^{-1} at disk center, and the wavelengths is in angstroms.

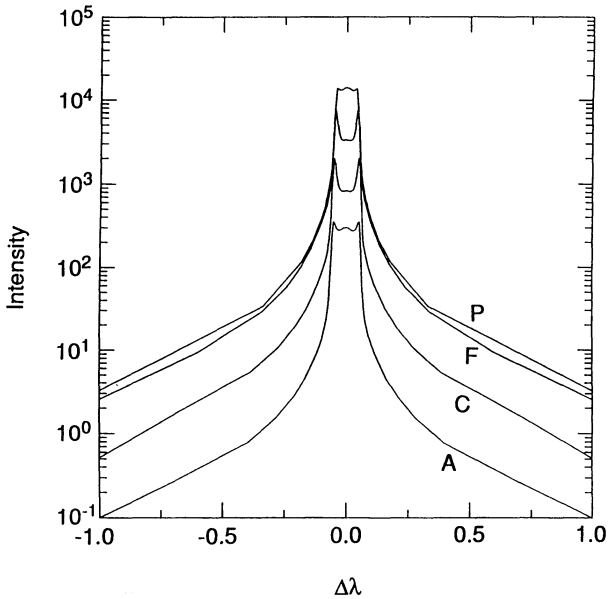

FIG. 13.—He I 584 Å line profile for models A, C, F, and P

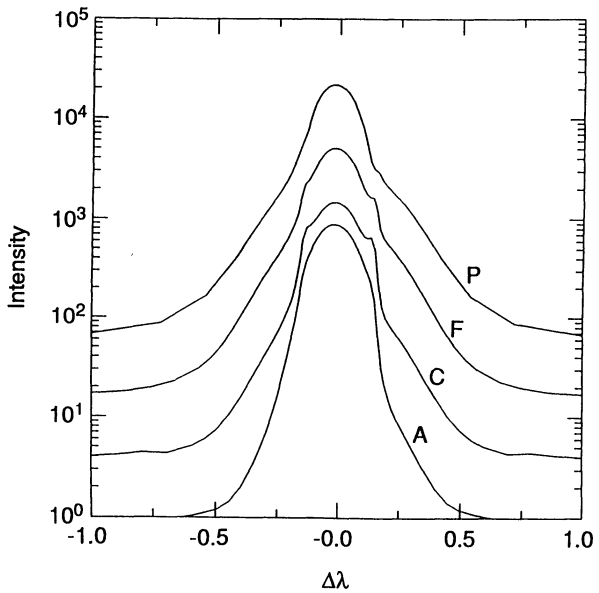

FIG. 15.—H 1026 Å (Lyβ) line profile for models A, C, F, and P

In contrast, the 584 Å He I resonance line (Fig. 13) shows a central reversal in most cases because of the effects of large optical thickness. This central reversal has different characteristics from that of the H Lyα line (Fig. 14), even though the shifted peaks of the 584 Å line originate at about the same levels of the upper chromosphere where the Lyα line peaks originate. The central reversal of the 584 Å line essentially disappears for both models A and P as a result of two different processes. In the case of model A the high-temperature underionized material has a very small optical thickness at line center so that the line core originates at the top of the chromosphere in a region of almost constant source function (largely dependent on our upper chromospheric model). In models C and F the line center forms at around 20,000 K, in the low transition region, where the source function decreases from the upper chromospheric values. In the case of model P the line center forms at temperatures higher than 20,000 K, but the source function does not decrease from the upper chromospheric values because of the higher density and the more rapid increase in temperature. In other words, in the weakest features the high-temperature underionized region does not substantially contribute to the line-center intensity because of its small optical thickness, and in the brightest features this hot region has near-unity optical thickness and the photons generated there are responsible for the line-center emission. In the intermediate-brightness models, the hot region has insufficient

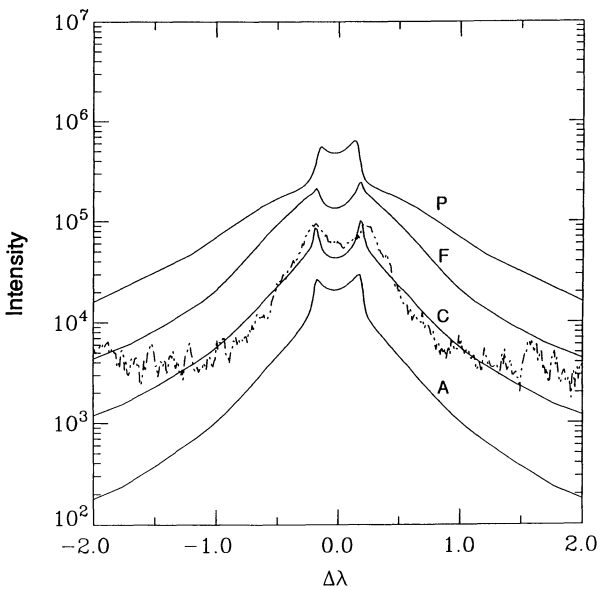

FIG. 14.—H 1216 Å (Lyα) calculated line profile for models A, C, F, and P, and an observed profile for the average quiet Sun from Fontenla, Reichmann, & Tandberg-Hanssen (1988) (*broken line*).

TABLE 5

CHARACTERISTICS OF THE CALCULATED LINES

Model	Line (Å)	$\int I_\nu d\nu$	I_c	FWHC	I_p	WPP	FWHP
A	1216	1.8E4	2.1E4	0.520	3.0E4	0.352	0.445
	1026	200	880	0.213	...	...	...
	584	40	300	0.120	350	0.102	0.118
	304	440	7.4E3	0.058	...	...	...
C	1216	6.3E4	4.4E4	1.000	9.9E4	0.370	0.544
	1026	395	1.5E3	0.236	...	...	...
	584	160	830	0.126	2.0E3	0.100	0.114
	304	920	1.5E4	0.059	...	...	...
F.....	1216	2.3E5	1.4E5	1.212	2.5E5	0.357	0.842
	1026	1.4E3	5.0E3	0.211	...	...	...
	584	600	3.3E3	0.115	7.4E3	0.087	0.106
	304	2.7E3	4.6E4	0.056	....	...	...
P.....	1216	5.2E5	4.9E5	0.488	6.4E5	0.270	0.418
	1026	6.1E3	2.1E4	0.198	...	...	...
	584	1.4E3	1.4E4	0.094	...	...	...
	304	1.5E4	2.7E5	0.056	...	...	...

NOTE.—$\int I_\nu d\nu$: Integrated intensity at disk center (ergs cm^{-2} s^{-1} sr^{-1}). I_c: Line-center intensity at disk center (ergs cm^{-2} s^{-1} sr^{-1} Å^{-1}). FWHC: Full width at half of central intensity (Å). I_p: Peak intensity at disk center (ergs cm^{-2} s^{-1} sr^{-1} Å^{-1}). WPP: Full width between peaks (Å). FWHP: Full width at half of peak intensity (Å).

optical thickness to enhance the source function at or above the chromospheric peak value. The FWHM for this line is model-dependent and changes from 0.1 to 0.12 Å for models P to C, and then decreases again to about 0.11 for model A. The line width of the 584 Å line is reported by Doschek, Behring, & Feldman (1974) to be about 0.14 Å. The observed integrated intensity from the quiet Sun is 545 ergs cm^{-2} s^{-1} sr^{-1} according to Mango et al. (1978). Our calculated values are somewhat low: 40 (A), 160 (C), and 600 (F).

The H Lyα line in Figure 14 shows the typical behavior we have described in Paper II, but has peaks that are higher and slightly more shifted, and wings that are more developed than in the earlier calculation, because of the increased upper chromospheric temperature we have adopted in our current models. The difference is substantial; the present profiles agree much better with observations, and we obtain an integrated intensity identical to the observed value for the average quiet Sun. The increased contribution of the wings (at more than 0.15 Å from line center, formed in the upper chromosphere at temperatures below 13,000 K) to the integrated emission accounts for about 75% of the total (for model C). This result shows that the Lyα line cannot be considered as a purely transition-region line but has an important upper chromospheric contribution. Figure 14 includes an observed disk-center profile for the average quiet Sun obtained by Fontenla, Reichmann, & Tandberg-Hanssen (1988) with the UVSP instrument on 1980 September 18 from an average over a 180″ slit. This profile has been corrected for geocoronal absorption.

The peak, central, and integrated line intensities are given in Table 5. The central intensities of the UV lines change from models A–P by a factor between 25 and 50 depending on the line. Although the values we compute for model C are below the observed quiet-Sun values for both the 304 and 584 Å lines, our model F results are within the observed range. While further adjustments of the models seem needed, part of the differences may be attributable to the large contrast between bright and dark features in the EUV and to the dominant influence of the bright features in spatially averaged observations. Support for this interpretation is provided by the values given by Vernazza & Reeves (1978) for (1) coronal hole intensities, which are closer to our model C results, and (2) network intensities, which are smaller than our model P results. Also, it should be noted that in some cases the contributions to the integrated intensity from the extended wings of the lines are substantial (although not as much as for H Lyα). Figure 15 shows the H Lyβ profiles that we compute from the four models. The intensity and profile of this line are highly model-dependent. Also note the asymmetry that is entirely due to the hydrogen diffusion velocity. The line center has its maximum contribution at about 30,000 K in all models, but the line wings beyond 0.1 Å from line center have increasing contributions from the upper chromosphere for models A–P. However, in contrast to the Lyα line, these extended wings (which vary over two orders of magnitude between models) only account for 20% of the integrated intensity in model P, and are entirely negligible for model A. Comparison with observations for this line is difficult because there are no high-sensitivity, high–spectral-resolution observations available where the effects of geocoronal absorption and line blends can be fully corrected. Also, the presence of some neutral hydrogen above the transition-region layers, which has been suggested by Schmahl & Orrall (1979), may produce some central absorption of the Lyβ line profile.

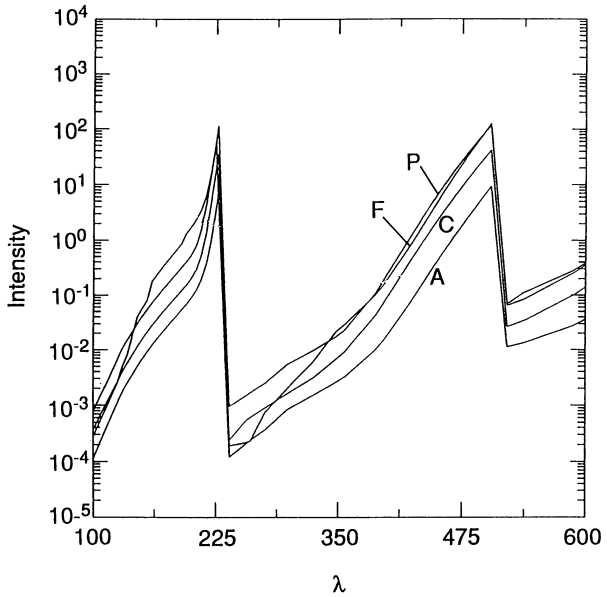

FIG. 16.—Helium continua for models A, C, F, and P

Figures 16 and 17 show the UV continua from He I and He II and from H, respectively. Note that the changes in intensity between models A and P are about a factor of 20, and that in all models the different continua overlap to some extent. These continua are strongly dependent on the adopted chromospheric temperature variation, and therefore we do not consider them in detail in this paper, but we note that the computed H and He I continua for models A, C, and F are in reasonably good agreement with the *Skylab* observations given in Table 8 of VAL III. Our computed model C intensity at the head of the He II continuum agrees with the value of about 10^{-12} ergs cm^{-2} s^{-1} sr^{-1} Hz^{-1} reported by Linsky et al. (1976). Note that in this case the differences between the model A, C, and F intensities are much less than for the 304 and 584 Å

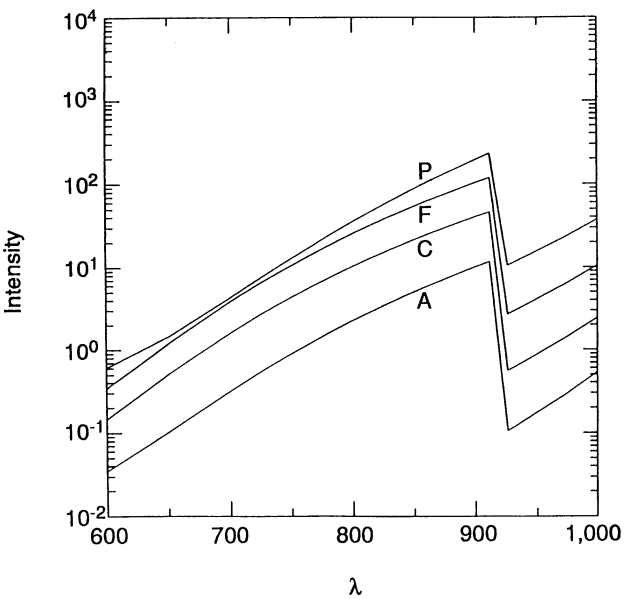

FIG. 17.—Lyman continuum for models A, C, F, and P

lines. Thus, if the models are correct, spatially averaged observations of the continuum should be close to the results calculated with model C, while such observations of the two resonance lines should lie between the model C and model F calculations. Our results roughly agree with the observations in this sense.

In Figure 18 we plot the He I 10830 Å line, i.e., the resonance line of the triplet series, normalized to the continuum intensity. This line is important for solar activity diagnostics, and we find that this absorption occurs in an optically thin region in the upper chromosphere. We find that this 10830 Å absorbing region in the upper chromosphere is highly affected by radiation incident from the upper transition region and corona as discussed in the next section. There we show why the model P line absorption is unexpectedly less than that of model C instead of greater than that of model F. Because of the different intensities adopted for the incident coronal radiation, these 10830 Å variations are not clearly related to the model temperature distributions.

The 1640 Å line, i.e., the He II Balmer-α line, is shown in Figure 19. We find that our calculations are not in agreement with the observations of this line. The continuum intensity at 1640 Å is formed in the temperature minimum region (according to VAL and the current models). Our model C has a minimum temperature of 4400 K (see Avrett 1985) in order to be consistent with the measured IR intensities and with the intensity minima in the near wings of the Ca II H and K lines. The computed Si I continuum around 1640 Å tends to have a slightly higher brightness temperature than 4400 K, and does not match the absolute intensity observations. The situation improves if there is a substantial reduction of the intensity due to absorption by a large number of lines. We currently use the line opacities of Kurucz (1991), assuming the source function corresponding to these line opacities to be a combination of thermal radiation and scattering. (See Anderson 1989, p. 575). So far we have been unable to find the appropriate combination of line-opacity and scattering effects that lead to full agreement with available observations. Consequently, our present calculations have uncertain local continua. In all our models the 1640 Å line is optically thin (which is consistent with the observations), but the calculated line intensity above the continuum tends to be substantially smaller than observed.

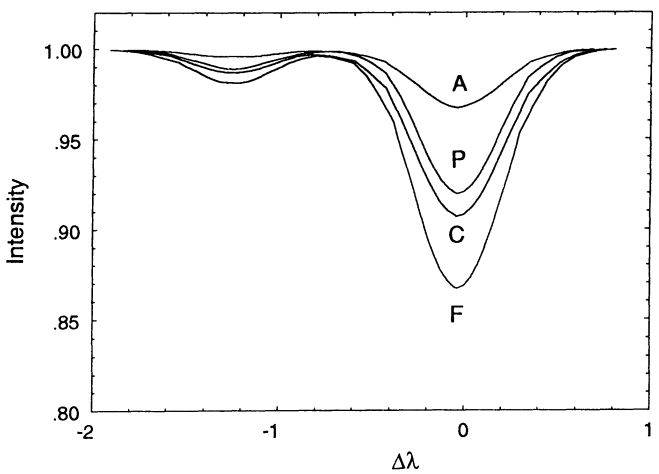

FIG. 18.—He I 10830 Å line profile (intensity relative to the continuum) for models A, C, F, and P.

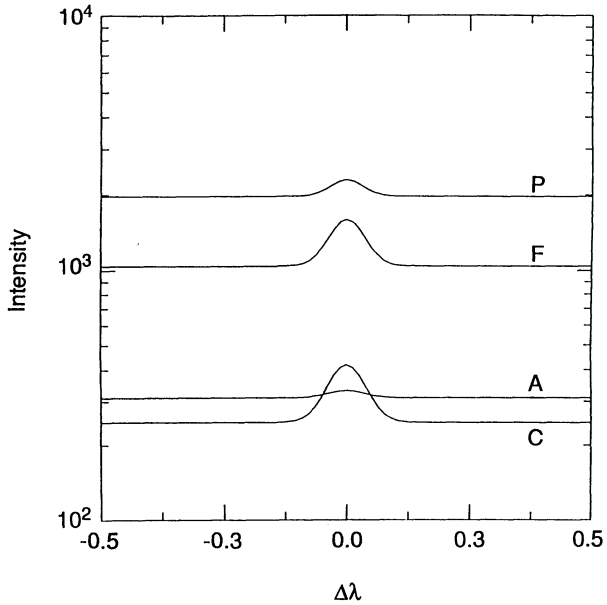

FIG. 19.—He II 1640 Å line for models A, C, F, and P

The reason for this discrepancy is uncertain, and it seems to us that the observed He II 1640 Å line has a larger intensity than one might expect for a subordinate line of its type, and that the large intensity may be produced by radiative pumping of the upper level by some shorter wavelength transition (e.g., by some highly ionized Fe coronal lines overlapping one of the resonance He II lines).

We have compared the line profiles from our models with those determined from the same $T(z)$ but where the statistical equilibrium equations were solved ignoring diffusion. We find substantial differences in the H and He I lines, but only small changes (less than 10%) in the continuum intensities and in the He II lines. The major change in the H Lyα and He I 584 Å lines is that by ignoring diffusion the central reversals become much more pronounced. The resulting central intensities without diffusion are factors of 2.8 and 1.8 smaller for the Lyα and He I 584 Å, lines, respectively, in our calculations for model C. These low central intensities are similar to those in the VAL calculations and have never been observed in any solar feature. The decreased central intensity does not greatly affect the Lyα integrated intensity (which decreases only by 12%), but it does affect the He I 584 Å line by a factor 0.67. Also, the effect of ignoring diffusion is rather important for the Lyβ line, whose peak and integrated intensities decrease by factors of about 3 and 2, respectively, when diffusion is ignored. In addition, ignoring diffusion substantially decreases the He II number density throughout the upper chromosphere. This has an important effect on the He I triplet populations and affects the 10830 Å line, whose central depression changes from 4% ignoring diffusion to the 9% of our model C calculation including diffusion.

6. EFFECTS OF INCIDENT CORONAL RADIATION

The calculations discussed in this paper include incident radiation from the coronal lines in the H, He I, and He II continua. We have not taken account of the strong coronal lines that are blended with the He II resonance lines at 256 Å, 243 Å, 237 Å,... (Linsky et al. 1976). The incident intensity data we use are obtained from the observed solar irradiances com-

piled by Tobiska (1991), who gives separate estimates of the irradiance contributions from coronal source regions and from the deeper layers (transition region and chromosphere). These contributions are differentiated on statistical rather than direct observational grounds because they are based on full-disk irradiance measurements. Also, Tobiska gives data for periods of low and moderate solar activity. Table 6 lists his irradiances from coronal source regions for low and moderate activity converted to the mean intensity at the solar surface. We use the low- and moderate-activity full-disk average as representative local values that are applied to our models A and C, respectively. For models F and P we use three times the moderate activity values. The mean intensity values at wavelengths other than the values listed in Table 6 are obtained by linear interpolation of the mean intensity as a function of frequency. The calculated monochromatic optical depths are used to attenuate these incident intensity values to give the incident contribution to the mean intensity at any depth in the atmosphere.

We have studied the influence of the incident intensity on our model C to determine how a change in the incident intensity affects the temperature dependence with height and the hydrogen and helium line and continuum emission. For this purpose we have constructed models CL and CH in addition to model C. Model CL is computed using the same transition-region boundary conditions as in model C, except for the use of the lower incident intensity, as in model A. Model CH has the same parameters as model C except for the use of the higher incident intensity, as in models F and P. The underlying chromospheric run of $T(z)$ was assumed to be the same for models CL and CH as for model C, but the transition regions of models CL and CH were independently calculated.

We found that the temperature structure of the transition region is not changed substantially by changing the incident radiation. But we find changes in the upper chromospheric electron density and particularly in the hydrogen and helium ionization in the upper chromosphere. Figure 20 shows that the combined H and He radiative losses in the upper chromosphere (at temperatures close to 8000 K) change drastically

TABLE 6

INCIDENT INTENSITY FROM CORONAL LINES

WAVELENGTH (Å)	MEAN INTENSITY (ergs cm^{-2} s^{-1} sr^{-1} Hz^{-1})	
	Low Activity	Moderate Activity
≤9.....	0	0
24.....	6.22E−16	1.47E−14
40.....	7.61E−16	1.74E−14
75.....	1.58E−14	5.30E−14
125.....	8.97E−15	1.99E−14
175.....	2.83E−13	8.04E−13
225.....	9.93E−14	7.30E−13
275.....	5.83E−14	1.37E−12
325.....	1.65E−13	2.16E−12
375.....	5.27E−13	1.27E−12
425.....	8.00E−14	2.24E−13
475.....	1.50E−13	4.74E−13
525.....	1.01E−14	2.15E−13
575.....	0	0
625.....	3.05E−13	9.23E−13
675.....	4.64E−14	7.01E−13
725.....	0	0
775.....	2.47E−13	6.11E−13
≥825.....	0	0

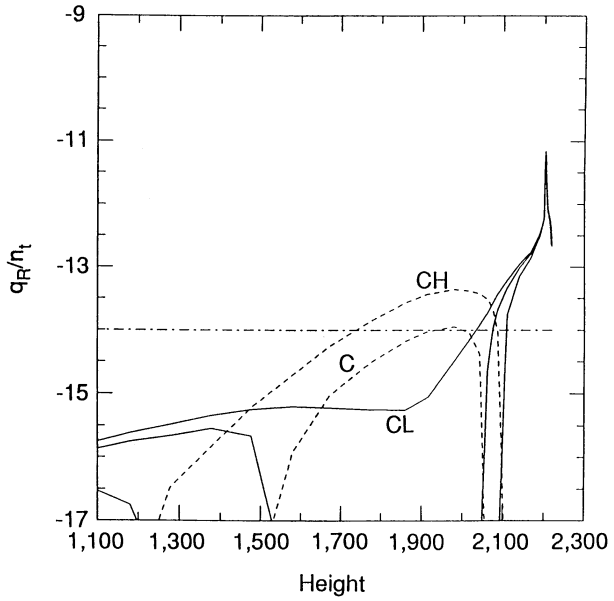

FIG. 20.—Radiative losses from the upper chromosphere for models CL, C, and CH, which have different incident coronal radiation. The solid line corresponds to positive values, the dashed line to negative values, and the dash-dot line to the estimate of the radiative losses from Anderson & Athay (1989).

between the three models with different incident intensities. The model with lowest incident intensity, model CL, has positive radiative losses per hydrogen atom of about 5×10^{-15} ergs cm^{-2} s^{-1} at 2000 km height and about 10 times less at lower heights. The value at 2000 km is comparable to the 10^{-14} value suggested by Anderson & Athay (1989) to characterize the chromospheric radiative losses. (They also include other element losses.) However, model C with the intermediate values of coronal incident radiation has very different radiative losses in this region; these losses are negative, which implies radiative heating, and are of about -10^{-14} ergs cm^{-2} s^{-1} per atom. Model CH, with higher incident coronal intensities that may be typical of network regions, has the higher radiative heating of about -4×10^{-14} ergs cm^{-2} s^{-1} per atom. The horizontal line in Figure 20 corresponds to the Anderson & Athay estimate; thus for high incident intensity the radiative heating or "backwarming" compensates and exceeds the radiative losses estimated by these authors over a height range of about 300 km (roughly at temperatures between 7000 and 8000 K). The electron densities in cm^{-3} at height 2000 km (temperature about 8000 K) are 3.5×10^{10} (CL), 4.4×10^{10} (C), and 5.7×10^{10} (CH).

These figures show that there is a substantial response of the upper chromosphere as a result of changes in the coronal UV irradiation. These changes occur because the hydrogen and helium ionization balance is affected by the intense coronal lines in the H and He continua. Changing the degree of ionization changes the radiative losses and therefore the energy balance of the upper chromospheric layers, which switch from being radiatively cooled by H and He emission into being heated through absorption of radiation from above (backwarming). These effects cannot be treated by the effectively thin approximation and must be modeled by using more sophisticated methods that include the backwarming, e.g., by detailed non-LTE radiative transfer computations. The radiative losses we show here are due only to H and He; other elements including C, Mg, and Fe are also major contributors

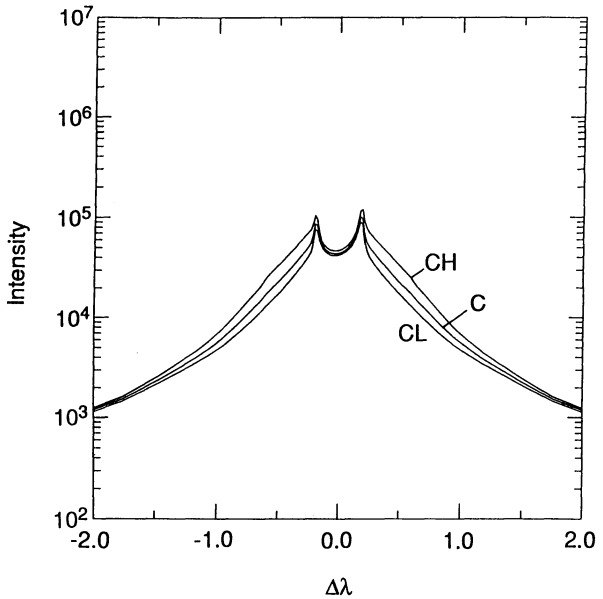

FIG. 21.—H 1216 Å (Lyα) line profile for models CL, C, and CH

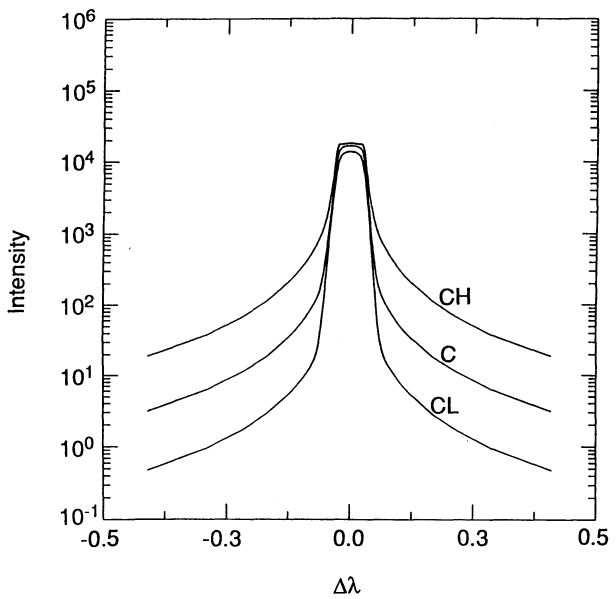

FIG. 23.—He II 304 Å line profile for models CL, C, and CH

in the upper chromosphere, and their radiative losses have to be taken into account to obtain the total loss estimates. The effects of coronal lines on these other elements should also be evaluated to assess whether increased incident intensity would lead to increased upper chromospheric temperatures even in the absence of additional local energy dissipation.

The effects of the incident radiation upon the emitted intensities are shown in Figures 21–26. Figure 21 shows the Lyα line profiles for models CL, C, and CH. As shown in this figure, some substantial changes (notice the logarithmic scale) occur in the wings of the line where the intensity increases by a factor of about 2 between model CL and model CH. More significant changes are shown in Figure 22 for the He I resonance line at 584 Å. This figure shows changes in the wings by a factor of about 6 but also displays changes in the line core. The core of this line changes from a basically flat profile (with three very small peaks) for model CL to one with a flat center and two strong peaks in the wings for model C, and to a self-reversed profile resembling that of Lyα for model CH. The integrated intensity also changes substantially for this line. Figure 23 shows that the He II resonance line at 304 Å (He II Lyα) has extremely large changes of the wing intensity, by a factor of about 40, and small changes in the line center, whose shape evolves from round self-absorbed emission to flat-topped saturated emission. This line never showed signs of self-reversal in any of the models we computed. The change in the integrated emission of this line is highly dependent on bandwidth because of the very extended wings it displays, particularly in the case of high incident intensity. Comparing with observations, we find that the intensities we compute are lower than the values

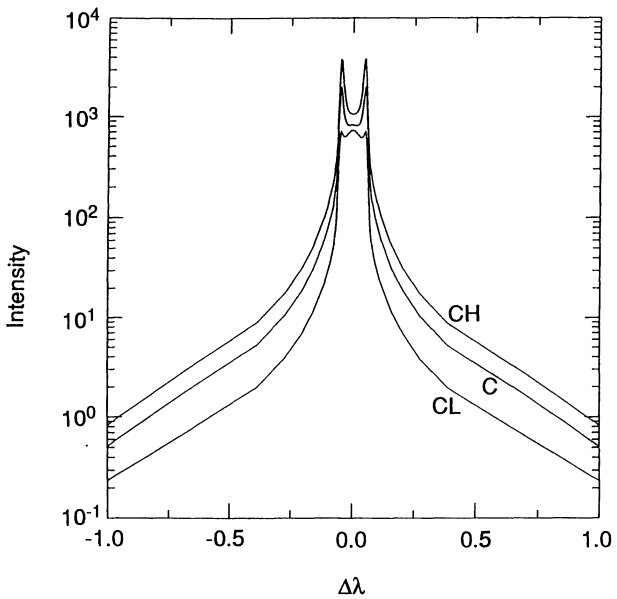

FIG. 22.—He I 584 Å line profile for models CL, C, and CH

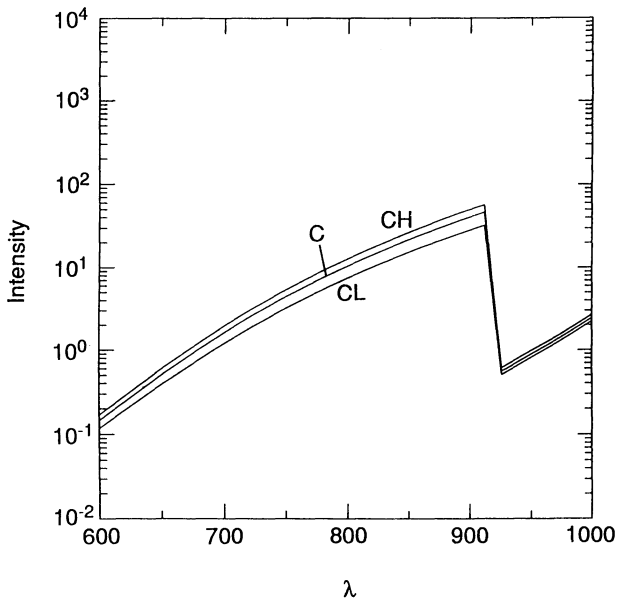

FIG. 24.—Lyman continuum for models CL, C, and CH

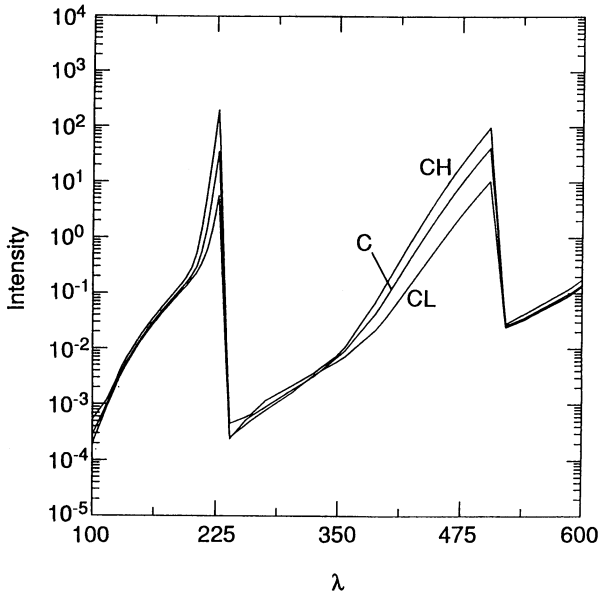

FIG. 25.—Helium continua for models CL, C, and CH

reported by some authors, but they coincide with some observed values. The discrepancy between different observations is due to difficulties with absolute calibration, and may also be affected by the presence of active regions in some cases; for a discussion of the observations see Linsky et al. (1976).

Figures 24 and 25 show the changes in the hydrogen Lyman continuum and the He I and He II continua, respectively. These figures show that while the changes in the Lyman continuum are small, the changes in the He continua are very substantial (again note the logarithmic scale). Note that we have omitted in these plots the contribution of the coronal lines to the total emitted intensity. Since this coronal line contribution is assumed to be optically thin, it should be added to obtain the total calculated emission to compare with the observations. We show in Figure 26 the He I 10830 Å line calculated for models CL, C, and CH. This line is very sensitive to the incident intensity because the increase in He I ionization increases the triplet level populations near the top of the chromosphere as shown in Figure 27, which causes greater absorption of the

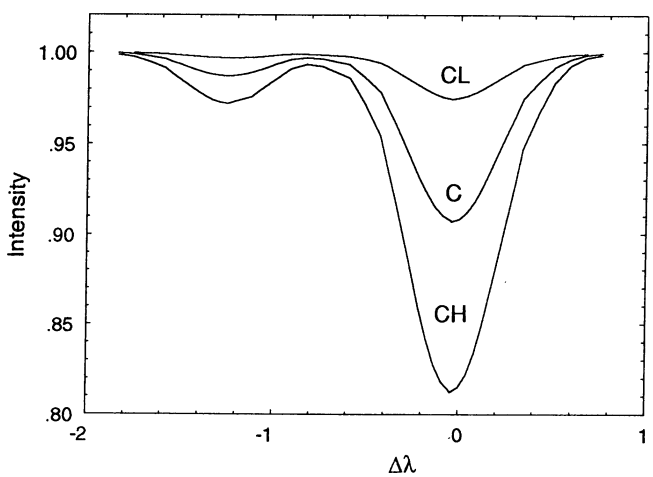

FIG. 26.—He I 10830 Å line for models CL, C, and CH

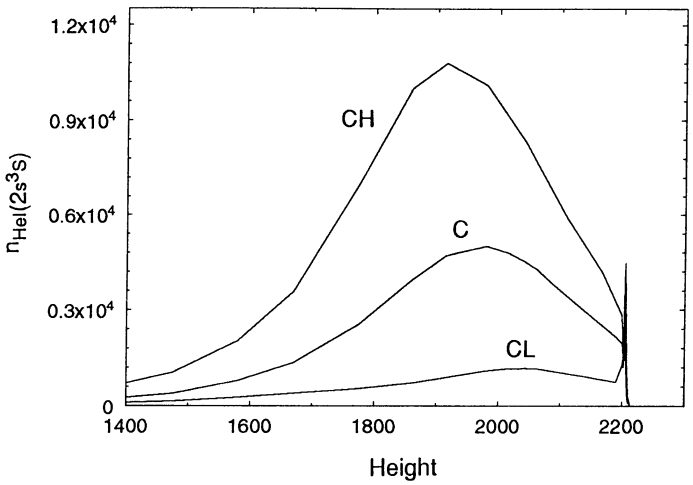

FIG. 27.—Number density (cm^{-3}) of the $2s\ ^3S$ level of He I vs. height (km) calculated for models CL, C, and CH.

continuum intensity at 10830 Å. The 10830 Å line-center optical thickness between 1400 and 2200 km is 0.042 (CL), 0.17 (C), and 0.37 (CH) in the three cases. These optical thicknesses are proportional to the areas under the three curves in Figure 27.

Figure 28 shows the calculated triplet level populations for models A, C, F, and P. The transition region is at a different height in each model. The maximum value of the $2s\ ^3S$ number density in the chromosphere is larger for model F than for model CH in Figure 27, even though the incident radiation is the same, because the total number density is larger in the upper chromosphere for model F. However, the integrated $2s\ ^3S$ number density of model F is smaller because the transition region is located deeper and because the attenuation of the $\lambda < 504$ Å ionizing radiation in the lower chromosphere is roughly the same in the two cases. The integrated $2s\ ^3S$ number density of model P is less than that of model F for the same reasons. The total chromospheric line-center optical thicknesses are 0.054 (A), 0.17 (C), 0.26 (F), and 0.15 (P).

We arbitrarily chose the coronal illumination for model F and for model P to be three times that of model C. As a result,

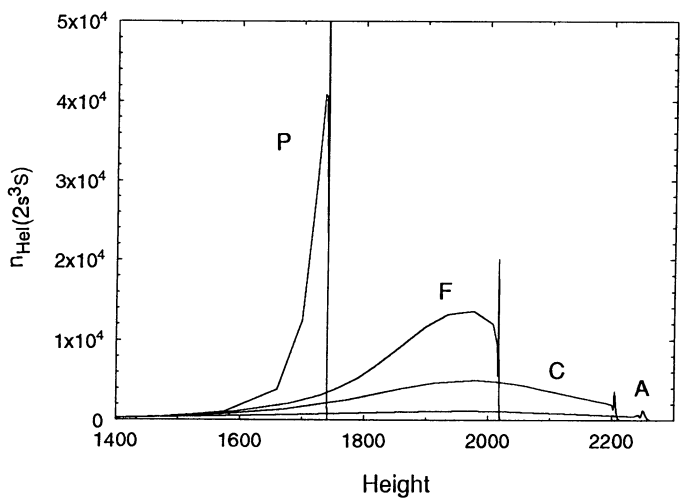

FIG. 28.—Number density (cm^{-3}) of the $2s\ ^3S$ level of He I vs. height (km) calculated for models A, C, F, and P.

the 10830 Å line of model P is found to be weaker than that of model C because of the reduced geometrical thickness of the chromosphere of model P. Since observations of plage regions show more absorption at 10830 Å than do observations of quiet regions, model P needs to be modified either by increasing the chromospheric scale heights in some way or by increasing the coronal illumination. We believe that the illumination values used in model P should be increased substantially, but have not yet carried out such calculations. Further discussion of how the 10830 Å line is formed appears in Avrett, Fontenla, & Loeser (1993).

7. CONCLUSIONS

We have carried out a detailed analysis of the effects of helium diffusion on our non-LTE radiative transfer and statistical equilibrium calculations. We have shown how diffusion causes He I ionization to be slightly greater in the upper chromosphere and substantially lower in the transition region, compared with local ionization calculations which ignore the effects of diffusion. These effects are similar to those found for hydrogen in our Papers I and II. The diffusion of the different ionization stages of He also influences the He II number density, but these effects are more complex. We found that diffusion greatly changes the He I resonance line emission, but has a less important effect on the He II lines. The importance of diffusion for the ionization balance was suggested by Shine, Gerola, & Linsky (1975) as a way to explain the observed He I and He II line intensities.

Our energy-balance calculations show that diffusion accounts for the central intensity of all the hydrogen and helium resonance lines. This seems to be the only mechanism proposed so far that explains the magnitude of the central reversals of these lines; the plateaus suggested by VAL accounted for the total intensity but gave extremely low central intensities and much larger reversals than observed. We also find that upper chromospheric emission contributes substantially to the integrated Lyα intensity but not much to the 584 Å He I line. Our results show how specific line profiles and line strengths depend on pressure and on incident radiation from coronal lines. We find that the frequently observed 10830 Å He I line depends both on pressure and on incident radiation.

In general, we find that our computed EUV line profiles and intensities are consistent with the observed ones (e.g., Vernazza & Reeves 1978; Doschek et al. 1974; Mango et al. 1978). However, more detailed simultaneous observations of the 304, 584, and 1216 Å lines at high spatial resolution would give significant insight on the conditions of the low transition region and upper chromosphere. Also, detailed analysis of the Mg II resonance lines would increase our understanding of the upper chromosphere, especially in view of the recent calculations by Uitenbroek (1991) which show that the emission cores of these lines have the same problem as the H and He I resonance lines when diffusion is ignored, viz., the computed central reversal is far too deep compared to the observed.

The diffusion coefficients used in our calculations are given in the Appendix. These coefficients are derived from kinetic calculations, based on momentum expansions, of St.-Maurice & Schunk (1977a, b) and Gueiss & Burgi (1986). Similar methods have also been applied by Woods & Holzer (1991) for mid–transition-region calculations of C IV line formation, abundance variations, and ion temperature structure for cases involving mass flows. The Woods & Holzer calculations do not determine the electron temperature versus height relation by an energy-balance calculation but use a somewhat arbitrary electron temperature stratification. Their models take into account the differences between the electron and ion kinetic temperatures, which are likely to occur in the upper layers of the transition region for the conditions they consider.

Our formulation for the diffusion is rather general (whenever first-order departures from a Maxwellian distribution are applicable) and includes mass flows and time-dependent effects in the equations. However, in this paper we only show numerical results for hydrostatic models (except for the inclusion of turbulent pressure) in which the atmosphere is assumed to be in a steady state and the "mass velocity" and differential flows are zero. Moreover, the models we show here assume constant helium abundance throughout the photosphere, chromosphere, and transition region, even though our formulation does not require a constant abundance. We have solved a few cases relaxing these assumptions, but the results are not included here (except as described briefly below) because the effects of mass flows and abundance variations require further studies and much further discussion. Here we mainly address the effects of helium diffusion on the emission from the transition region and upper chromosphere for hydrostatic cases with energy balance between particle energy downflow and radiative losses, assuming a constant helium abundance. We have shown that the characteristic times for achieving a stationary state are smaller than the characteristic times of observed variations and that the one-dimensional approximation is valid locally because of the small vertical scale of the transition region compared with the scale of the observed variations across the disk. From these considerations, it is clear that our present calculations apply to regions of the solar atmosphere in which mass flows and differential flows are negligible, and local energy dissipation in the transition region is small compared with the radiative losses that balance the particle energy downflow from hot coronal regions. These conditions seem appropriate for the footpoints of hot coronal loops such as are shown in many recent observations (e.g., Golub et al. 1990).

We now comment on the important problem posed by possible helium abundance variations. Our preliminary calculations show that important abundance variations can be produced by ambipolar diffusion. This occurs because the helium (either neutral or ionized) particle momentum is more strongly coupled to the inward-diffusing ions than to the outward-diffusing neutrals. Therefore, in a steady state, the helium abundance must decrease outward to avoid a net helium inflow. This effect is expected for any element that is neutral at the base of the transition region (viz., having a high first-ionization potential). For elements that are already ionized at the base of the transition region (low first-ionization potential) the effect of thermal diffusion (see Appendix, eq. [A20]) would tend to balance the effect of ambipolar diffusion.

The expected abundance variations for high first-ionization potential elements would be substantially moderated by any mass flows, even the very small mass flows that account for the solar wind. However, the problem of helium abundance is a very complicated one because of the uncertainty of the required boundary conditions and especially because, in contrast to the ionization times, the characteristic times for abundance changes over extended atmospheric regions may be larger than or comparable to the typical time variations of observed features. In a subsequent paper we will investigate in detail how ambipolar diffusion induces a decreased coronal

abundance of helium and other elements with a high first-ionization potential.

We are grateful to the referee, Lawrence S. Anderson, for very helpful comments. This research was supported by the Space Physics Division of the NASA Office of Space Science and Applications (grant NAGW-2096 to J. M. F. and grant NSG-7054 to E. H. A.).

APPENDIX

THE DIFFUSION OF HELIUM IN THE SOLAR ATMOSPHERE

Here we will explain in detail the theoretical basis for our equations (14)–(16) and the method we use to estimate the helium diffusion coefficients d which are used in equation (16).

In the present study we assume that the presence of helium does not significantly affect the diffusion of hydrogen atoms, protons, and electrons. Consequently, we will use equations (3.1) and (3.2) of Paper I to describe the ambipolar diffusion, i.e., the relative diffusion of hydrogen atoms with respect to electron-proton pairs (we neglect any small change due to the presence of helium ions). Also, we will assume as before that the electric current is zero, and that an equilibrium electric field (thermoelectric field) has been set up by space-charge buildup. This electric field is obtained from the first-order expansion of the distribution function shown in Appendix B of Paper I, and results in a linear expression that depends on the temperature and hydrogen-ionization gradients. (The gravity and pressure gradient effects are negligible for the transition region.) This equilibrium electric field is important for ionized helium diffusion (as will be shown later) and is given by

$$E_0 = -e[r_T \nabla \ln T + r_x \nabla \ln (n_p/n_a)] \quad \text{(A1)}$$

where e is the proton charge, n_p is the proton number density, and n_a is the neutral hydrogen atom density. The coefficients we use are given by a fit to the numerical values computed by Fontenla, Ferro Fontan, & Rovira (1989, hereafter FFR). The fit gives

$$r_T = T[430 + 110(x + 0.5)/x] , \quad r_x = T[300/(x + 0.5)] \quad \text{(A2)}$$

with all quantities in cgs units and $x = n_p/n_a$. These expressions for the thermoelectric and ionic-electric coefficients were calculated using the formalism given in the Appendix B of Paper I, and are described in more detail by FFR. The expressions given in equation (A2) are only valid for $x > 0.1$ and for typical conditions of the solar atmosphere; for very low ionization values the coefficients depart from these equations. Also, we have neglected the electric field due to the gravitational force, since this force is small compared with that caused by the temperature gradient. The coefficients in equation (A2) were determined assuming that the depth variation of the pressure $p_x = (n_H + n_p)kT$ is negligible. These coefficients permit us to compute the self-consistent electric field of equation (A1) that would result from the temperature and ionization gradient after the electric current has vanished (see Braginskii 1965). We find that for most solar transition region conditions the electric field E_0 is very close to that given by Braginskii (1965) and Spitzer (1962) for a fully ionized plasma. This occurs despite the substantial departure from full ionization of the low transition region layers; we find that significant departures from the Braginskii and Spitzer values only occur in the solar atmosphere at the much lower ionization degree characteristic of the low chromosphere.

We treat helium diffusion in the same way as hydrogen based on first-order departures from Maxwellian distributions (see MacNeice, Fontenla, & Ljepojevic 1991). This approach results in linear functions of the gradients in all thermodynamic parameters (see Paper I). We carry out the calculations in the local center-of-mass frame (the "fluid frame"). Here, in contrast to the approach we used in Paper I, we do not compute the departure from Maxwellian distributions in detail. Rather, we use the momentum conservation equation for each species (e.g., see Braginskii 1965) and a momentum expansion of the kinetic (Boltzmann) equations for all species following the procedure used by Gueiss & Burgi (1986, hereafter GB) which is based on methods developed by St.-Maurice & Schunk (1977a, b, hereafter SMS). However, we note that this treatment is only approximate because it was not developed in detail for the mixture we are considering here, in which all stages of helium ionization are present, and because several simplifying assumptions are made. Nevertheless, the differences regarding the gas mixture may not lead to significant errors here because we are only interested in the behavior of minor species. A more critical issue is that in methods based on moment expansions of the kinetic equations we must resort to truncation of higher order momenta of the distribution function. The accuracy of this truncation is very difficult to assess and can only be determined by a more complicated detailed numerical solution of the kinetic equations, such as the one we have used before (see our Paper I) for hydrogen diffusion. The method we apply here, though imprecise, gives a reasonable first approximation to the particle diffusion and can be expressed by analytical formulae. In our present calculations we neglect inelastic collisions (involving excitation/de-excitation and ionization/recombination), and as usual we assume that the phenomena of interest occur on temporal scales much larger than those for elastic collisions, and on spatial scales much larger than the mean free path. Also, in our present treatment we assume a common temperature for all species. This contrasts with the case considered by Woods & Holzer (1991) for the higher temperature fully ionized layers with mass flows. In the cases we are considering, the temperatures of the different species are likely to be very similar because of the high density, and any first-order differences in these species temperatures are probably unimportant for our study.

Using the momentum equations (A6), (A7), and (A11) of Paper I for each helium species, we obtain

$$m_s\left[\frac{\partial(n_s V_s)}{\partial t} + \nabla \cdot (n_s V_s V_s)\right] + \nabla \cdot \Gamma_s + \nabla p_s - m_s n_s g - n_s Z_s e\left(E + \frac{V_s \times B}{c}\right) = P_s , \quad \text{(A3)}$$

where the index s designates a given helium species (He I, He II, or He III), and where we include for reference the viscous stress and magnetic field terms which subsequently will be neglected. In this equation Γ_s is the viscous tensor, E is the electric field, B is the magnetic field, g is the gravitational acceleration, and V_s

is the diffusion velocity. V_s, g, E, B, and P_s (see below) are all vectors. The right-hand side of equation (A3) is the first moment of the collisional term in the corresponding Boltzmann equation (see Paper I),

$$P_s = \int p\xi_s \, dp^3 , \tag{A4}$$

where p is the vector corresponding to the particle momentum. In our present study we assume that the time derivative of the distribution function, the quadratic term in the diffusion velocity, the viscosity, and the magnetic field terms are all negligible compared with the terms due to spatial variations of temperature, density, and ionization. Further, we neglect the effect of gravity for the transition region, and we also neglect the radiative pressure effects mentioned in Paper I, so that

$$\sum_s P_s = 0 . \tag{A5}$$

Using the expression for the Boltzmann collision term, it can be easily shown that the net momentum gain of a given species can be expressed in terms of the momentum exchange with the other species

$$P_s = \sum_t P_{st} , \tag{A6}$$

where the rate of momentum exchange, P_{st}, is a linear function of the first-order departures from Maxwellian of the two species s and t. This rate can be obtained from the classical expression of the Boltzmann collision term (see Chapman & Cowling 1936),

$$P_{st} = \int dp_s^3 \, p_s \int dp_t^3 \, v_{st} \int d\sigma_{st}(f_s f_t - f_s' f_t') , \tag{A7}$$

where f_s and f_t are the corresponding distribution functions for the two species which are colliding, and the prime values are the corresponding ones after the collision. Since the momentum is conserved in elastic collisions, the momentum gained by one species is lost by the other, so that

$$P_{st} = -P_{ts} . \tag{A8}$$

For a two-species gas the quantities P_{st} for the momentum exchange can be regarded as friction forces (or, better, dynamic friction forces) between the species s and t, and can be expressed in terms of the difference between the diffusion velocities of the two species and the thermal force (e.g., see Braginskii 1965) as

$$P_{st} = -C_{st}(V_s - V_t) + D_{st} \nabla \ln T , \tag{A9}$$

where the two coefficients, C_{st} and D_{st}, depend on the collision cross sections. The first coefficient is proportional to the reduced mass, m_{st}, and the product of both species number densities, n_s and n_t. The second coefficient is proportional to the partial pressure of the species s. With these assumptions, we can write the momentum equation for each of the helium species as

$$\nabla p_s - n_s Z_s E_0 e = -C_{sa}(V_s - V_a) - C_{sp}(V_s - V_p) - \sum_t C_{st}(V_s - V_t) + D_s \nabla \ln T , \tag{A10}$$

where the indices a and p refer to neutral hydrogen atoms and protons, respectively, and where the s and t indices refer to helium species. The collisions with electrons have been neglected because the momentum transfer between electrons and heavy particles is very small. The total cross sections necessary for determining the coefficients are computed including the angular projection factor and are often called "momentum exchange cross sections,"

$$\sigma_{st} = \int (1 - \cos \chi) d\sigma , \tag{A11}$$

where χ is the deflection angle commonly used in the analysis of collisions. However, the coefficients C_{su} not only include these total cross sections but also must include the corrections which arise due to the dependence of the momentum exchange on the relative velocity of the colliding particles. These corrections are evaluated following SMS and GB. According to these papers, we can express the momentum gained by the species s as

$$P_s = -\sum_u n_s m_s \nu_{su}(V_s - V_u) + \sum_u \nu_{su} \frac{z_{su} m_{su}}{kT} \left(q_s - \frac{n_s m_s}{n_u m_u} q_u \right) , \tag{A12}$$

which is identical to equation (14) of GB. The index u in this equation includes all hydrogen and helium species, and q_s represents the corresponding species heat fluxes. The z_{su} coefficients are estimated from the approximate dependence of the cross sections on the velocity: $z_{su} = -\frac{1}{5}$ for hard spheres (used in neutral-neutral collisions), $z_{su} = \frac{3}{5}$ for Coulomb collisions (used for ion-ion collisions), and $z_{su} = 0$ for induced dipole-type collisions (used for ion-neutral collisions). The collisional rates are calculated using the collision cross sections as

$$\nu_{su} = (m_{su}/m_s) n_u \langle V\sigma \rangle_{su} . \tag{A13}$$

Following the equations given by SMS and GB, the species heat fluxes (see also eqs. [A9] and [A10] in Paper I) can be expressed in terms of the velocity differences and the temperature gradient with the aid of several approximations (one of these is the truncation of the moments). The approximations are characterized by equations (17)–(20) in GB. The full expressions including the three helium species, hydrogen atoms, and protons are very complicated. However, we are principally interested in a gas composed mainly of partially ionized hydrogen and only small fractions of other minor species. The solar helium abundance is not so small that we can treat helium as a trace species. Thus we had to modify the GB formulation and believe that in this way we obtain a reasonable order-of-magnitude estimate for an otherwise extremely complicated problem. We characterize helium diffusion by the equations

$$\nabla p_s - n_s Z_s E_0 e = P_s , \tag{A14a}$$

where

$$P_s = -C_{sa}(V_s - V_a) - C_{sp}(V_s - V_p) - C_{sap}(V_p - V_a) - \sum_t C_{st}(V_s - V_t) + D_s \nabla \ln T . \tag{A14b}$$

The coefficients in this equation are given by

$$C_{su} = n_s m_s \nu_{su}(1 - \Delta_{su}) ,$$
$$C_{sap} = n_s m_s (\nu_{sp} \Delta'_{sp} - \nu_{sa} \Delta'_{sa}) , \tag{A15}$$
$$D_s = p_s \alpha_s ,$$

and the coefficients α_s are given by equations (59) and (60) of GB. Using equations (57) and (58) of GB, we find that the corrections to the momentum exchange between species terms

are given by

$$\Delta_{st} = (v_{st}/v'_{st})(5z_{st})^2 , \tag{A16}$$

where the v'_{st} are defined by GB equations (61) and (62). The additional term in equation (A14b) that does not appear on the right-hand side of equation (A10) arises from the velocity dependences of the cross sections and is proportional to the difference of the diffusion velocities of protons and atoms, which is just the hydrogen diffusion velocity, V_A. (V_A is equal to the negative ambipolar diffusion veocity for a pure hydrogen gas.) This additional term corresponds to diffusion of helium induced by the hydrogen diffusion, and the coefficients can be found from equations (57) and (58) of GB, giving

$$\Delta'_{sa} = \frac{5z_{sa}\, z_{ap}\, A v''_a}{4(A+1)D}\left(1 - \frac{27 v_{sa}}{v'_s} + \frac{20 v''_p\, v_{sp}}{v''_a\, v'_s}\right),$$
$$\Delta'_{sp} = \frac{5z_{sp}\, z_{ap}\, A v''_p}{4(A+1)D}\left(1 - \frac{27 v_{sp}}{v'_s} + \frac{20 v''_a\, v_{sa}}{v''_p\, v'_s}\right), \tag{A17}$$

where A is the atomic mass (of helium in this case) relative to hydrogen, and the remaining quantities are described in GB. Note that we use the indices a and p instead of 0 and 1 used by GB, and we use the letter V instead of u for designating the species diffusion velocity. The remaining notation is the same, and the index s corresponds to x for neutral helium and y for singly or doubly ionized helium.

Note that the diffusion velocity of neutral relative to ionized hydrogen, V_A, is not strictly the same as the "ambipolar diffusion velocity" $V_{\rm amb}$ in the multicomponent gas we treat here. However, when the gas is mainly composed of hydrogen, V_A is very close to the ambipolar diffusion velocity (with opposite sign according to some definitions; see Papers I and II), which can be expressed as

$$V_{\rm amb} = \frac{m_{\rm H} n_p V_p + m_{\rm He}(n_{\rm II} V_{\rm II} + 2n_{\rm III} V_{\rm III})}{m_{\rm H} n_p + m_{\rm He}(n_{\rm II} + 2n_{\rm III})} - \frac{m_{\rm H} n_a V_a + m_{\rm He} n_{\rm I} V_{\rm I}}{m_{\rm H} n_a + m_{\rm He} n_{\rm I}} . \tag{A18}$$

Note also that there are small differences between our equations (A14) and the GB equations (57) and (58). The differences are that (1) we have neglected the inelastic (or reactive) collisions and therefore we do not include a term involving γ_{st}, and (2) we have included the elastic collisions between helium species which were not included in the GB equations. This is only a small difference because the added terms are small, but we think that including them might somewhat improve the accuracy of the calculations. The rationale for this is that we assume that the inclusion of momentum transfer by elastic collisions between helium species may somewhat affect the net momentum gain of a given helium species, and this effect can be described by terms of the form

$$n_s m_s \nu_{st}(V_s - V_t)(1 - \Delta_{st}) . \tag{A19}$$

But we assume that the inclusion of these collisions between helium species would not seriously affect the heat fluxes of the main species (hydrogen atoms, protons, and electrons), and the expressions for Δ'_{sa} and Δ'_{sp} remain basically unchanged. Of course, this procedure may be questioned because it is not fully self-consistent, but we believe that in view of the crudeness of several other approximations made (e.g., regarding the values of z_{su}), the loss of accuracy due to neglecting some of the minor effects is inconsequential.

The next step is to convert equations (A14) to a form similar to equations (16) (in the main part of this paper), and therefore to provide the proper definitions for the coefficients d_{st}. For this purpose we first express the species diffusion velocities in terms of the independent set of "relative diffusion velocities" defined by equations (14). This is accomplished by replacing the species diffusion velocities using equations (17), and gives the following set of equations

$$\nabla p_{\rm I} - D_{\rm I}\nabla \ln T = \left(C_{1ap} + \frac{n_p C_{1a} - n_a C_{1p}}{n_{\rm H}}\right)V_A - (C_{1a} + C_{1p})V_B - (C_{1a} + C_{1p})\frac{(n_{\rm II} + n_{\rm III})V_C + n_{\rm III} V_D}{n_{\rm He}} - (C_{12} + C_{13})V_C - C_{13} V_D , \tag{A20a}$$

$$\nabla p_{\rm II} - n_{\rm II} E_0 e - D_{\rm II}\nabla \ln T = \left(C_{2ap} + \frac{n_p C_{2a} - n_a C_{2p}}{n_{\rm H}}\right)V_A - (C_{2a} + C_{2p})V_B + (C_{2a} + C_{2p})\frac{n_{\rm I} V_C - n_{\rm III} V_D}{n_{\rm He}} + C_{21} V_C - C_{23} V_D , \tag{A20b}$$

and

$$\nabla p_{\rm III} - 2n_{\rm III} E_0 e - D_{\rm III}\nabla \ln T = \left(C_{3ap} + \frac{n_p C_{3a} - n_a C_{3p}}{n_{\rm H}}\right)V_A - (C_{3a} + C_{3p})V_B + (C_{1a} + C_{1b})\frac{n_{\rm I} V_C + (n_{\rm I} + n_{\rm II})V_D}{n_{\rm He}} + C_{31} V_C + (C_{31} + C_{32})V_D . \tag{A20c}$$

Expressions for the gradients of the partial pressures in terms of the helium ionization, helium abundance, hydrogen density, and temperature gradients can be found by using the relations

$$\begin{aligned} p_{\rm He}/p_{\rm I} &= 1 + (n_{\rm II}/n_{\rm I})[1 + (n_{\rm III}/n_{\rm II})] , \\ p_{\rm He}/p_{\rm II} &= (n_{\rm I}/n_{\rm II}) + 1 + (n_{\rm III}/n_{\rm II}) , \\ p_{\rm He}/p_{\rm III} &= (n_{\rm II}/n_{\rm III})[(n_{\rm I}/n_{\rm II}) + 1] + 1 , \\ p_{\rm He} &= (n_{\rm He}/n_{\rm H})p_{\rm H} . \end{aligned} \tag{A21}$$

We use these relations, together with equation (A1), to express the left-hand side of equations (A20) in terms of the variables listed in equations (15), assuming that the total pressure (the sum of p_e, $p_{\rm H}$, and $p_{\rm He}$) remains practically constant. The procedure we use is a numerical inversion and multiplication of matrices rather than an analytical derivation, which would be cumbersome. However, we have given all the details needed to obtain the diffusion coefficients in terms of well-known theory.

The remaining point concerns the actual values of the collisional rates we have used. For the collisions between neutral helium particles we have used the formula for the rate given by GB, which is

$$\langle V\sigma\rangle = 8 \times 10^{-10} \tag{A22}$$

in cgs units. This rate is not very well known, but its role is minor. For the collisions between neutral helium and hydrogen we estimate a value

$$\langle\sigma\rangle = 8 \times 10^{-16} T_4^{-0.7} \quad \text{(A23)}$$

from some published values (e.g., Newman et al. 1986), where T_4 is the temperature in units of 10,000 K. Using this estimate, we conclude that the corresponding collisional rate has only a very weak temperature dependence and can be expressed as

$$\langle V\sigma\rangle = 10^{-9} T_4^{-0.2} . \quad \text{(A24)}$$

This value is only an estimate, but it is fully compatible with the published measurements. The cross sections for collisions which involve one ion are larger, and better known and documented. The collisions between neutral and ionized helium are obtained from Janev et al. (1987), and we used the following fits to the data shown by these authors

$$\langle V\sigma\rangle = 2 \times 10^{-9} T_4^{0.25}/(2.5 + T_4^{0.2}) \quad \text{(A25)}$$

for He-He$^+$ collisions, and

$$\langle V\sigma\rangle = 2 \times 10^{-9}(1 - 0.1 \log_{10} T_4) T_4^{0.4} \quad \text{(A26)}$$

for He-He^{++} collisions.

For collisions between protons and neutral helium, and between ionized helium and hydrogen, we used a fit to numerical values of the cross sections computed by Kimura (1991). Using these and the approximation

$$\langle V\sigma\rangle \approx \langle\sigma\rangle[1.6 \times 10^{12}(m_H/m) T_4]^{1/2} , \quad \text{(A27)}$$

we obtain the collisional rates

$$\langle V\sigma\rangle = 0.9 \times 10^{-7} T_4^{1/2}/(1 + 0.43 T_4^{1/2}) \quad \text{(A28)}$$

for H-He$^+$ collisions, and

$$\langle V\sigma\rangle = \frac{4 \times 10^{-9}[(2.8662 - 0.25613 X_4) X_4 - 1]}{1 - 1.25013 X_4 + 0.140843 T_4 - 1.31387 T_4^{-1/2}} , \quad \text{(A29)}$$

where $X_4 = \log_{10} T_4$, for He-H$^+$.

The remaining relevant cross sections, for H-He^{++} and for He-H$^+$, are not well studied but are not very critical for this work because the regions containing substantial amounts of one of the particles do not contain much of the other. Anyway, we have derived estimates of these collision rates by assuming that these collisional rates are similar to other better known rates. For H-He collisions (assumed to be similar to He-He collisions) we use

$$\langle V\sigma\rangle = 8 \times 10^{-10} . \quad \text{(A30)}$$

For H-He^{++} (assumed to be similar to the collision rate for H-H$^+$, from Janev et al. 1987, but four times larger) we use

$$\langle V\sigma\rangle = 33.6 \times 10^{-9}(1 - 0.14 \log_{10} T_4) T_4^{0.4} . \quad \text{(A31)}$$

These rates, especially the last, are probably overestimated, but we do not regard this as a serious problem in our calculations, and we will improve these rates in our models as soon as more accurate data become available. To evaluate some coefficients in equations (55) of GB which affect our equations (A17), we also need the collision rate between neutral hydrogen atoms. For this we use a fit to the cross sections shown by Massey (1971) and mentioned in Paper I. The expression we use is

$$\langle V\sigma\rangle = 2.26 \times 10^{-9}[1 - (1.1 - T_4^{0.25})^2] . \quad \text{(A32)}$$

For the ion-ion collisions we have adopted the formula (after Braginskii 1965)

$$\langle V\sigma\rangle_{su} = \frac{4}{3} 0.85 \frac{\ln\Lambda}{10} \frac{Z_s^2 Z_u^2}{T^{3/2}} \left(\frac{m_H}{m_{su}}\right)^{1/2} . \quad \text{(A33)}$$

Note that the values of z_{su} taken from GB and used in equation (A12), not to be confused with Z_s in equation (A33), are not fully consistent with the specific forms of the variations of the cross sections with collision velocity which we find in the literature for the collisions involving neutral particles, and these coefficients may substantially affect the collisional terms C_{su} in some cases. Therefore, the present treatment is only approximate. More accurate results would be obtained by a full treatment such as the one we used in Paper I for hydrogen and described in more detail by FFR. However, our present results should give order-of-magnitude estimates that are sufficient to show the significance of the different processes and to give a first approximation to the effects of helium diffusion.

Instead of using the methods we develop here, it also should be possible to solve equation (A14) for the species diffusion velocities. However, by using our approach based on equations (A20) and "relative diffusion velocities," one can easily avoid inconsistencies due to numerical effects that are hard to avoid in a solution of equations (A14). This difficulty occurs because equations (A3) constitute a nonlinear, integrodifferential set of coupled equations whose solution must satisfy several tight constraints, e.g., mass, momentum, and energy conservation; see above and Paper I. Moreover, the constraints consist of differential equations whose solution depends on boundary conditions. Using our method developed here and in Papers I and II, we are able to solve all these constraining equations subject to clearly stated, physically plausible boundary conditions, assuming a steady state. At the same time we solve the species diffusion equations by a fully consistent approach, up to first order in the departures from Maxwellian distributions; see Paper I. The validity of this first-order approximation has been verified for our models by MacNeice, Fontenla, & Ljepojevic (1991).

REFERENCES

Anderson, L. S. 1989, ApJ, 339, 558
Anderson, L. S., & Athay, R. G. 1989, ApJ, 346, 1010
Athay, R. G. 1990, ApJ, 362, 364
Avrett, E. H. 1985, in Chromospheric Diagnostics and Modelling, ed. B. W. Lites (Sunspot: National Solar Observatory), 67
Avrett, E. H., Fontenla, J. M., & Loeser, R. 1993, in IAU Symp. 154, Infrared Solar Physics, ed. D. M. Rabin & J. T. Jefferies (Dordrecht: Kluwer), in press
Braginskii, S. I. 1985, in Reviews of Plasma Physics (New York: M. A. Leontovich Consultants Bureau), 205
Cally, P. S. 1990, ApJ, 355, 693
Chapman, S., & Cowling, T. G. 1936, The Mathematical Theory of Nonuniform Gases (Cambridge: Cambridge Univ. Press)
Cox, D. P., & Tucker, W. H. 1969, ApJ, 157, 1157 (CT)
Cushman, G. W., & Rense, W. A. 1978, Sol. Phys., 58, 299
Doschek, G. A., Behring, W. E., & Feldman, U. 1974, ApJ, 190, L141
Fontenla, J. M., Avrett, E. H., & Loeser, R. 1990, ApJ, 355, 700 (Paper I)
———. 1991, ApJ, 377, 712 (Paper II)
Fontenla, J. M., Ferro Fontan, C., & Rovira, M. 1989, unpublished manuscripts, available from authors (FFR)
Fontenla, J. M., Reichmann, E. J., & Tandberg-Hanssen, E. 1988, ApJ, 329, 464

Golub, L., Herrant, M., Kalata, K., Lovas, I., Nystrom, G., Pardo, F., Spiller, E., & Wilczynski, J. 1990, Nature, 344, 842
Gueiss, J., & Burgi, A. 1986, A&A, 159, 1 (GB)
Janev, R. K., Langer, W. D., Evans, K., Jr., & Post, D. E., Jr. 1987, in Elementary Processes in Hydrogen-Helium Plasmas, ed. G. Eckes, P. Lambropoulos, & H. Walther (New York: Springer)
Jordan, C. 1975, MNRAS, 170, 429
Kimura, M. 1991, private communication
Kurucz, R. L. 1991, in Stellar Atmospheres: Beyond Classical Models, ed. L. Crivellari, I. Hubeny, & D. G. Hummer (Dordrecht: Kluwer), 440
Lemaire, P., Gouttebroze, P., Vial, J.-C., & Artzener, G. E. 1981, ApJ, 103, 160
Lindsey, C., & Jefferies, J. T. 1990, ApJ, 349, 286
Linsky, J. L., Glackin, D. L., Chapman, R. D., Neupert, W. M., & Thomas, R. J. 1976, ApJ, 203, 509
MacNeice, P., Fontenla, J. M., & Ljepojevic, N. N. 1991, ApJ, 369, 544
Maltby, P., Avrett, E. H., Carlsson, M., Kjeldseth-Moe, O., Kurucz, R. L., & Loeser, R. 1986, ApJ, 306, 284
Mango, S. A., Bohlin, J., Glackin, D. L., & Linsky, J. L. 1978, ApJ, 220, 683
Massey, H. S. W. 1971, Electronic and Ionic Impact Phenomena, Vol. 3 (Oxford: Clarendon)
Newman, J. H., Chen, Y. S., Smith, K. A., & Stebbings, R. F. 1986, J. Geophys. Res., 91, 8947
Schmahl, E. J., & Orrall, F. Q. 1979, ApJ, 231, L41
Schunk, R. W. 1975, Planet. Space Sci., 23, 437
Shine, R., Gerola, H., & Linsky, J. L. 1975, ApJ, 202, L101
Spitzer, L. 1962, Physics of Ionized Gases (New York: Interscience)
St.-Maurice, J.-P., & Schunk, R. W. 1977a, Planet. Space Sci., 25, 243 (SMSa)
———. 1977b, Planet. Space Sci., 25, 907 (SMSb)
Tobiska, W. K. 1991, J. Atm. Terr. Phys., 53, 1005
Uitenbroek, H. 1991, in ASP Conf. Ser., Vol. 26, Seventh Cambridge Workshop on Cool Stars, Stellar Systems, and the Sun, ed. M. Giampapa & J. A. Bookbinder (San Francisco: ASP), 564
Vernazza, J. E., Avrett, E. H., & Loeser, R. 1981, ApJS, 45, 635 (VAL)
Vernazza, J. E., & Reeves, E. M. 1978, ApJS, 37, 485
Woods, T. D., & Holzer, T. E. 1991, ApJ, 375, 800